

Contents lists available at ScienceDirect

Acta Biomaterialia

journal homepage: www.elsevier.com/locate/actbio



Full length article

Molecular weight of hyaluronic acid crosslinked into biomaterial scaffolds affects angiogenic potential



Josh Karam^a, Breahna J. Singer^{a,b}, Hiromi Miwa^a, Limin H. Chen^b, Kajal Maran^a, Mahdi Hasani^a, Sarahi Garza^a, Bianca Onyekwere^a, Hsin-Chih Yeh^{b,c}, Song Li^a, Dino Di Carlo^a, Stephanie K. Seidlits^{a,b,*}

- ^a Department of Bioengineering, University of California, Los Angeles, CA 90095, USA
- b Department of Biomedical Engineering, The University of Texas at Austin, Austin, TX 78712, USA
- ^c Texas Materials Institute, The University of Texas at Austin, Austin, TX 78712, USA

ARTICLE INFO

Article history: Received 8 March 2023 Revised 29 July 2023 Accepted 1 August 2023 Available online 10 August 2023

Hyaluronic acid Hydrogels Wound healing Angiogenesis CD44

ABSTRACT

While hyaluronic acid (HA)-based hydrogels have been used clinically for decades, the mechanisms by which HA exerts molecular weight-dependent bioactivity and how chemical modification and crosslinking may affect molecular weight-dependent bioactivity remain poorly understood. This knowledge gap presents a significant barrier to designing HA hydrogels with predictable bioactivities. As HA has been widely reported to have molecular weight-dependent effects on endothelial cells (ECs), we investigated how the molecular weight of HA in either soluble or crosslinked forms affects angiogenesis and interrogated CD44 clustering on the surface of endothelial cells as a candidate mechanism for these affects. Using soluble HA, our results show high molecular weight (HMW) HA, but not low molecular weight (LMW) HA, increased viability and tube formation in cultured human cerebral microvascular ECs (HCMVECs). No size of HA affected proliferation. When HCMVECs were cultured with crosslinked HA of varying molecular weights in the form of HA-based microporous annealed particle scaffold (HMAPS), the cell response was comparable to when cultured with soluble HA. Similarly, when implanted subcutaneously, HMAPS with HMW HA were more vascularized than those with LMW HA. We also show that antibody-mediated CD44 clustering resulted in HCMVECs with increased viability and tube-like structure formation in a manner comparable to exposure to HMW HA, suggesting that HMW acts through CD44 clustering.

Statement of significance

Biomaterials based on hyaluronic acid (HA), a bioactive extracellular matrix polysaccharide, have been used in clinical products for several years. Despite the knowledge that HA molecular weight heavily influences its bioactivity, molecular weight has been largely ignored in the development of HA-based biomaterials. Given the high viscosity of high molecular weight HA typically found in native tissues, lower molecular weight polysaccharides have been used most commonly for biomaterial fabrication. By comparing the ability of injectable, microporous annealed particle scaffolds (MAPS) fabricated from variably sized HA to promote angiogenesis, this study demonstrates that MAPS with high molecular weight HA better support vascularization, likely through an unique ability to induce clustering of CD44 receptors on endothelial cells.

© 2023 The Authors. Published by Elsevier Ltd on behalf of Acta Materialia Inc.

This is an open access article under the CC BY-NC-ND license (http://creativecommons.org/licenses/by-nc-nd/4.0/)

1. Introduction

Hyaluronic acid (HA) is a prominent glycosaminoglycan component of the extracellular and pericellular matrices throughout the body [1–3]. HA is composed of repeating disaccharide subunits of D-glucuronic acid and N-acetyl-D-glucosamine connected by β -

E-mail address: seidlits@utexas.edu (S.K. Seidlits).

^{*} Corresponding author.

glycosidic linkages that can be repeated up to thousands of times, yielding HA chains ranging from 0.8 kDa to 20,000 kDa [1,2]. To enable controlled crosslinking into hydrogels, HA polysaccharides can be easily functionalized with multiple reactive groups using aqueous, bio- and cyto-compatible chemistries [4,5]. Modification of HA is commonly done by functionalizing the carboxylic acid group on the glucuronic acid, which mediates binding to CD44, a major HA receptor [6]. Thus, high degrees of modification (>40%) can interfere with HA-CD44 interactions [7]. HA hydrogels have been used clinically in orthopedic and ophthalmologic applications for decades [5,8,9]. However, these early generation HA hydrogels were developed with consideration primarily for their physical properties, such as hydration, stiffness, and ease of crosslinking, rather than their bioactive properties [5,10]. More recently, researchers have recognized that altering the physical properties of HA hydrogels also may alter their bioactivity and directly affect phenotypes of interfacing cells [4,11-15]. Despite its simple chemical structure, HA exhibits molecular weight-dependent bioactivity [1,16-23]. A significant barrier to designing HA hydrogels as therapeutics with predictable bioactivities is a lack of understanding of the mechanisms by which HA exerts MW-dependent bioactivity and how chemical modification and crosslinking may affect MWdependent bioactivity. Addressing this knowledge gap will be critical to realize the full therapeutic potential of HA-based biomateri-

In normal, uninjured tissues, high molecular weight (HMW) HA is dominant and helps to maintain homeostasis. In contrast, a critical process throughout all phases of wound healing, which are traditionally characterized as hemostasis, inflammation, proliferation, and remodeling, is continual production and degradation of HMW HA into low molecular weight (LMW HA) fragments [1,3,24]. Platelets migrate towards an acute injury site and release HMW HA (>1000 kDa, HMW HA). This HMW HA is first degraded by hyaluronidase 2 (HYAL2) into approximately 20 kDa fragments, which act to initiate the inflammatory response [16,17,25-27]. HYAL2 activity decreases with fibrin clot formation, allowing HMW HA to accumulate and integrate into the main architecture of the provisional matrix [1,24]. As the provisional matrix forms, LMW HA fragments (≤70 kDa) continue to recruit neutrophils to the injury site [16,24,28,29]. Neutrophil infiltration into the provisional matrix is facilitated by the presence of HMW HA, which retains a high volume of water, swells the provisional matrix, increases porosity [24,30,31]. Once at the injury site, neutrophils producing free radicals and reactive oxygen species (ROS) that further degrade HMW HA [1,32,33]. During the inflammatory phase, LMW HA induce inflammatory cells to produce cytokines and chemokines which recruit additional monocytes/macrophages [1,3]. LMW HA also promotes polarization of macrophages towards a pro-inflammatory phenotype, which further reinforces the inflammatory signaling cascade [21,34]. In cases of chronic inflammation, LMW HA and various inflammatory cells persist in the injury site [1,24,35,36].

Together, cytokines/chemokines and LMW HA recruit fibroblasts, smooth muscle cells, and endothelial cells (ECs), which are necessary for the proliferation and remodeling phases of wound healing [1,33,37–39]. Monocytes, macrophages, and EC progenitors cooperate in neovascularization and forming granulation tissue, in the following proliferative phase [1,24]. Fibroblasts are stimulated to produce HMW HA, which promotes their proliferation when degraded into fragments of ≤70 kDa [37,40]. As the proliferation phase progresses, HYAL-mediated degradation of HA begins to decrease so that HMW presence is increased in granulation tissue [1,3]. As healing resolves, the HMW HA matrix is stored, fibroblasts and macrophages undergo apoptosis, and neovascularization ends, leaving behind restored tissue [1,24].

HA can act through both its HMW and LMW forms through CD44, a transmembrane protein found on the plasma membranes of almost all human cells [3,17]. The ability of HA to differentially bind to its receptors, including CD44 and CD168 (aka HMMR, RHAMM), and toll-like receptor 2/4 (TLR 2/4) in a MW-dependent fashion is widely believe to underlie varying cell responses to high and low MW HA polysaccharides [1-3,21,36,41,42]. While HMW HA remains extracellular, CD44 mediates internalization of 20 kDa HA fragments produced by HYAL2 degradation of HMW HA in a process contributing to wound healing [43,44]. For example, Jiang et al. showed that blocking HA-CD44 binding in macrophages impaired clearance of LMW HA and resulted in delayed healing in a mouse model of lung inflammation [45]. In vitro studies have found that CD44 interactions with LMW HA also mediate migration towards and proliferation of various cell types, including fibroblasts and ECs, in the wound site [23,37,38,40,46]. In contrast, HMW HA helps maintain tissue homeostasis by preventing proliferation through CD44 binding [43,48,49]. However, researchers have yet to undercover the specifics of how HA molecular weight may differentially activate receptors. A prevailing theory among researchers is that the molecular weight-dependent bioactivity of HA relies on the presumed ability of its HMW forms to cluster CD44 receptors [50]. For example, CD44 clustering, in the presence of HMW HA, has been shown to block activation and downstream signaling of TLR 2/4 [16,51] and mediate Hippo signaling to regulate cell density-dependent growth [49].

HA also facilitates the stages of angiogenesis, a process required for wound healing. In vitro studies have reported that LMW HA promotes human umbilical vein ECs (HUVECs) proliferation and directed migration in the early phases of angiogenesis, whereas HMW HA inhibits HUVEC proliferation [19,23,46,47,52]. However, other studies have suggested that this view may be too simplistic [19,53]. For example, Lokeshwar et al. showed HA may have distinct effects on ECs from different tissues [19]. Specifically, they found that LMW HA (8-10 kDa) promoted proliferation of EC lines derived from aortic and venous tissues, but not ECs derived from microvascular lung tissue. Overall, the molecular weight-dependent effects of HA on angiogenesis are not yet fully understood. Implanted HA-based biomaterials have been widely reported to facilitate angiogenesis [54-59]; however, the timing and potency of these effects varies across biomaterial formulations [55,59,60]. We suspect that these differences could be accounted for by variations in chemical modification and molecular weight of

This study investigated how the molecular weight of HA incorporated into a crosslinked hydrogels may affect angiogenesis and wound healing. In addition, we explored how molecular weightdependent clustering of CD44 receptors may relate to molecular weight-dependent HA bioactivity. We assessed the effects HA molecular weight, in its soluble and crosslinked forms, on the angiogenic capacity of human cerebral microvascular ECs (HCMVECs). We investigated how crosslinking HA into a biomaterial affects its angiogenic activity using HA-based microporous annealed particle scaffolds (HMAPS). In its soluble and crosslinked forms, HMW HA promoted greater HCMVEC viability and vessel-like structure formation in vitro than did LMW HA, while no form of HA affected proliferation. When subcutaneously implanted into mice, HMAPS fabricated from HMW HA induced significantly greater scaffold vascularization than HMAPS fabricated from LMW HA. Finally, in vitro we demonstrate that in the absence of added HA, clustering of CD44 receptor using a bivalent antibody induced HMVEC phenotypes equivalent to those observed with exposure to HMW HA. Altogether, our data show that HA MW is an important variable in the design of HA-based hydrogels and that CD44 clustering is involved in HA molecular weight-dependent bioactivity.

2. Experimental methods

2.1. Cell culture

SV40-immortalized human cerebral microvascular endothelial cells (HCMVEC, Applied Biological Materials (ABM), T0259) at passage 6 or 7 were used for all endothelial cell experiments. HCMVECs were cultured in ScienCell's Endothelial Cell Media complete (ECMC, 1001) on either PriCoat flasks (ABM, G299) or Applied Cell Extracellular Matrix (ACECM, ABM, G422) coated plates per manufacturers' instructions. For all 2D solubilized HA experiments, cells were cultured in ECMC or ECM supplemented with 1 mg/ml HA (1M, 100K, 40K, 10K, or No HA) without the endothelial cell growth supplement. Lenti-XTM 293T (Takara, 632180) cells were cultured in DMEM (Genesee Scientific, 25-500) supplemented with 10% fetal bovine serum (Thermo Fisher Scientific, A3160502) and 1% antibiotic-antimycotic solution (Caisson Labs, ABL02-100ML).

2.2. EdU test for proliferation

HCMVECs were seeded in the appropriate media condition for 22 h before a 2 h incubation with 2'-Deoxy-5-ethynyluridine (EdU, Abcam, ab146186) for 2 h. At 24 h, EDU was removed and cells were passaged and fixed using 4% paraformaldehyde for 15 min. After fixation, cells are permeabilized using 0.1% saponin and 1% BSA in PBS. EdU staining was performed using the Click-iTTM Plus Alexa FluorTM 488 Picolyl Azide Toolkit (Thermo, C10641) per manufacturer's instructions. Flow cytometric analysis was performed using a Millipore Guava EasyCyte 5 HPL Benchtop Flow Cytometer and GuavaSoft.

2.3. Viability and apoptosis

HCMVECs were seeded in the appropriate media condition and cultured for 24 h in a 96-well plate before viability and apoptosis were measured using the ApoLive-GloTM Multiplex Assay (Promega, G6411). Viability is measured in this assay using glycylphenylalanyl-amino fluorocoumarin (GF-AFC), a cell-permeant peptide substrate that generates a fluorescent reading when cleaved by live-cell protease activity. Apoptosis is measured using a caspase 3/7 luminogenic substrate. Data is reported as the ratio of viable to apoptotic cells (RVAC)

2.4. Tube formation

Tube formation angiogenesis experiments were carried out using the angiogenesis 96-well μ -plates from Ibidi (89646). Wells were first coated with Geltrex LDEV-Free Reduced Growth Factor Basement Membrane Matrix (Thermo, A1413202). HCMVECs were then seeded in the appropriate media conditions and allowed to attach for 6 h. A Zeiss Axio Observer Z1 inverted fluorescence microscope was used to monitor tube formation, taking phase images every 10 min with a 4x objective for up to 24 h. Automated image analysis was then performed using the Tube Formation FastTrack AI Image Analysis (Ibidi, 32100).

2.5. Thiolated hyaluronic acid (HA-SH) synthesis and characterization

Sodium hyaluronate (41-65 kDa (40K, HA40K) and 750-1000 kDa (1M, HA1M), Lifecore Biomedical) was dissolved at 10 mg/mL in deionized (Di) $\rm H_2O$ and thiolated as previously described using 1-Ethyl-3-[3-dimethylaminopropyl] carbodiimide (EDC, Sigma-Aldrich, 03450-5G), N-hydroxysuccinimide (NHS, Sigma-Aldrich, 130672-5G), and cystamine dihydrochloride (Thermo Fisher Scientific, AAB2287314) to replace the carboxyl on HA with a disulfide bridge [61–64]. Disulfides are reduced using dithiothreitol

(DTT, Thermo Fisher Scientific, BP172-25). The molar ratios of EDC/NHS/cystamine/DTT to HA are listed in Table S2. HA-SH was purified using dialysis against acidic (pH 4) di $\rm H_2O$ for 3 days in the dark. Purified, HA-SH was vacuum filtered through a 0.22 μ m filter (EMD Millipore), frozen under liquid nitrogen, lyophilized, and stored at -20°C until use. HA thiolation (Table S1) was confirmed using the colorimetric Ellman's test for free thiols.

2.6. Microfluidics device fabrication

A flow-focusing microfluidic device was used for manufacturing hydrogel spheres. Microfluidic devices were fabricated using standard soft lithography techniques. Master molds were fabricated on mechanical grade silicon wafers (University wafer) using KMPR 1050 photoresist (Microchem). Devices were molded from the masters using poly(dimethyl)siloxane (PDMS) Sylgard 184 kit (Dow Corning). The PDMS base and crosslinker were mixed at a 10:1 mass ratio, poured over the mold, and degassed prior to curing overnight at 65°C. Channels were sealed by treating the PDMS mold and a glass microscope slide (VWR) with oxygen plasma at 500 mTorr and 80 W for 30 s. The channels were functionalized by injecting 100 μL of Aquapel and reacting for 30s until washed by Novec 7500 (3M). The channels were dried by air suction and kept in the oven at 65°C until used.

2.7. Hydrogel microparticle formation

HA-SH (0.75 wt% for 1M and 3 wt% for 40K) was crosslinked with 20 kDa vinyl sulfone-terminated 4-arm polyethylene glycol (PEG-VS, JenKem Technology, A7025-1) modified with 300 µM thiolated RGD (RGD-SH, GenScript) and 10 µM thiolated fluorophore, Flamma 552 (AdipoGen, BCT-CWT1058-M001). The ratio of SH:VS is 1.2:1 to allow for excess free thiols. These pre-gel solutions were sterile-filtered through a 0.2 µm polyethersulfone (PES) membrane in a luer lock syringe filter, injected into the microfluidic device, and pinched off by an oil phase (0.1% Pico-Surf in Novec 7500, Sphere Fluidics, SF-000149). The flow rate for aqueous solutions was 10 µL/min and for oil solutions was 50 µL/min. Microparticle gels were collected from the device in the oil phase and allowed to crosslink overnight at room temperature in the dark. Microgels were then vortexed with 20% 1H,1H,2H,2H-Perfluoro-1octanol (PFO) (Sigma-Aldrich) for 10s. Microgels were then mixed with a 1:1 mixture of HEPES buffer (100 \times 10 mM HEPES, 40 \times 10 mM NaCl pH 7.4) and hexane followed by centrifugation at 10,000 rpm for five minutes five times to separate microgels from oil. Microgels were incubated in sterile filtered 70% ethanol solution at 4°C overnight for sterilization. Before experiments, microgels were washed with HEPES buffer five times. For in vitro studies, microparticles were concentrated by centrifugation and incubated in the designated culture dish overnight at 37°C to allow the microparticles to anneal, forming an HA-based microporous annealed particle scaffold (HMAPS).

2.8. Mechanical characterization

Bulk gels made of the same solutions used for microparticle fabrication (HA-SH and PEG-VS modified with RGD and Flamma 552) were swollen to equilibrium overnight in PBS before mechanical characterization. An AR2000 rheometer (TA Instruments) with crosshatched plate and 8 mm geometry to prevent slipping and a solvent trap to minimize evaporation was used to perform oscillatory stress sweeps at 1 Hz and 1% strain and frequency sweeps at 1% strain. The testing stage was maintained at 37°C.

J. Karam, B.J. Singer, H. Miwa et al. Acta Biomaterialia 169 (2023) 228–242

2.9. Confocal imaging and immunofluorescence

HBMVECs were cultured in HMAPS using ECMC without ECGS. HMAPS cultures were performed using 8-well chambered polymer coverslips (Ibidi, 80826). After 48 h, cells were fixed using 4% paraformaldehyde in PBS (Santa Cruz Biotechnology, sc-281692), then permeabilized using 0.2% triton X-100 in PBS for 5 min. Cells were then incubated with Image-iTTM FX signal enhancer (Thermo Fisher Scientific, I36933) for 30 min and blocked with 4% normal donkey serum (Sigma-Aldrich, D9663) and 1% bovine serum albumin (Bioworld, 22070008) in PBS with 0.1% tween-20. Primary antibodies for pan-actin (1:50, ACTN05 (C4), Novus Biologicals, NB600-535) and ZO-1 (1:25, ZMD.437, Thermo Fisher Scientific, 40-2300) were incubated overnight at 4°C. Secondary antibodies Alexa fluor 488 conjugated donkey anti-mouse (1:1000, Thermo Fisher Scientific, A21202) and Alexa fluor 647 conjugated donkey anti-rabbit (1:1000, Thermo Fisher Scientific, A31573) and Hoescht 33342 (1:1000, Thermo Fisher Scientific, H3570) were then incubated with samples for 1 hour at room temperature. Imaging of HMAPS cultures was performed using a Leica SP5 laser scanning confocal microscopy system and a 5x objective. Z-stacks were taken with slices 2 µm apart. Max projections were generated using the Lecia LAS AF software.

2.10. In vivo subcutaneous injection

Female C57BL/6J mice (N = 3 implants per each of two scaffold conditions); The Jackson Laboratory), 6–8 weeks old, were anesthetized with 2.5% isoflurane using an inhalation anesthesia system. Each mouse received two subcutaneous injections of HMAPS beads suspended in 100 μL of PBS using an 18-gauge needle under the ventral interior panniculus carnosus, where in each mouse 1M HA HMAPS was delivered to the one side (right or left) and 40K HA HMAPS was delivered to the contralateral side. Mice were euthanized 9 days after HMAPS bead injection and HMAP implantation (along with surrounding subcutaneous tissue and muscle) were collected.

2.11. Immunohistochemistry of tissue sections

HMAPS/tissue explants were frozen in OCT and cryosectioned into 14 µm sections. Sections were post-fixed using 4% paraformaldehyde before permeabilization with 0.5% Triton X-100 in Tris-buffered saline (TBS). The sections were then incubated with Image-iTTM FX signal enhancer for 30 min and blocked with 10% normal donkey serum (Sigma-Aldrich, D9663) and 5% bovine serum albumin (Bioworld, 22070008) in TBS with 0.1% tween-20 (TBST). Sections were then incubated overnight at 4°C with rat anti-mouse CD44 (1:200, Thermo Fisher Scientific, 14-0441-86) and rabbit anti-mouse laminin (1:200, Thermo Fisher Scientific, PA1-16730) primary antibodies in blocking buffer. Sections were rinsed 3 times with TBST and incubated with donkey anti-rat Alexa Fluor 488 (1:1000, Invitrogen, A21208) and donkey antirabbit Alexa Fluor 647 (1:1000, Invitrogen, A31573) in blocking buffer for 1 hour at room temperature. Sections were stained with Hoescht 33342 (1:1000) for 2 min in Di H₂O and rinsed before mounting with Fluoromount-G® (Southern Biotech, 0100-01). Images of whole sections were acquired by tiling and stitching 20x images using a Zeiss Axio Observer Z1 inverted fluorescence microscope. Quantification was performed using the Zen 3.4 software (Zeiss) by drawing an ROI around the HMAPS implant, measuring the intensity sum, and normalizing it by the area of the ROI. For each implant (1 1M HMAPS and 1 40K HMAPS per animal, N=3 per scaffold condition), at least 2 sections were quantified.

2.12. Antibody-mediated crosslinking of CD44

The protocol for antibody-mediated crosslinking of CD44 was adapted from Ooki et al. [49] HCMVECs were trypsinized into a single cell suspension. After rinsing with PBS, HCMVECs were incubated at 37°C for 90 min with rat anti-human CD44 antibody (10 μ g/ml, Thermo Fisher Scientific, 14-0441-86). HCMVECs were then rinsed 3 times in culture media before incubation at 37°C for 60 min with goat anti-rat IgG Fc secondary antibody (10 μ g/ml, Thermo Fisher Scientific, 31226). HCMVECs were then seeded in the experimental conditions.

2.13. Vector design

All lentiviral vectors were developed using VectorBuilder's Vector Design tool and purchased from VectorBuilder. To perform all FRET studies, three vectors were developed: CD44-mTFP1 (VB210402-1113mts), CD44-Ypet (VB171201-1092vjt), and PMT-mTFP1-Ypet (VB210402-1112gew). To perform all western blot studies, a CD44 overexpression vector (VB191002-1258ayx) was developed. For creation of hCD44-Halo7, pEGFPN1-integrin β 1-SGX3-Halo7 was used as a backbone. pEGFPN1-integrin β 1-SGX3-Halo7 was a gift from Dr. Akihiro Kusumi [65]. Asc1 and BsrG1 were used to remove integrin β 1. hCD44 was cloned into the vector using HiFi DNA Assembly (New England Biolabs).

2.14. Lentivirus production

Briefly, 80% confluent HEK cells were transfected with third generation packaging plasmids (pRSV-Rev and pMDLg/pRRE were gifts from Didier Trono (Addgene plasmids # 12253 and # 12251, respectively)), a plasmid encoding the lentiviral capsule (pCMV-VSV-G was a gift from Bob Weinberg, Addgene plasmid # 8454), and either a CD44-mTFP1, CD44-Ypet, PMT-mTFP1-Ypet, or CD44 overexpression vector using jetPRIME transfection reagent (Polyplus transfection). Lentiviral particles were recovered from media after 2 days of culture using PEG-itTM virus precipitation solution (SBI System Biosciences), resuspended in 1x PBS and stored at – 80°C.

2.15. Acceptor-photobleaching-based FRET measurement

Confocal microscopy imaging and photobleaching experiments were performed at 37°C using a Leica SP5 laser scanning confocal microscopy system and a 63x water immersion objective, HC APO L 63x/0,90 W U-V-I (Leica, 506148). If there are any interactions between mTFP1 (donor) and Ypet (acceptor) leading to energy transfer in the cells, photobleaching Ypet would lead to an increase in mTFP1 intensity since mTFP1 would no longer be quenched by the Ypet. In the photobleaching experiments, a high intensity laser (100% laser power at 514 nm beam) was applied to the region of interest for 500 frames to locally bleach the Ypet present. Data acquisition was gathered immediately after bleaching. The sample area was scanned at the resolution of 1024×1024 pixels. The mTFP1 and Ypet were excited at 458 and 514 nm, respectively. Two frames of pre-bleach and post-bleach mTFP1 and Ypet fluorescence intensities were recorded. The FRET efficiency € was calculated using the following equation:

$$E = 1 - (F_{pre}/F_{post})F_{pre}$$

The variables F_{pre} and F_{post} indicate the fluorescent intensity of mTFP1 before and after acceptor photobleaching, respectively. All FRET Efficiency measurements were made using the FRET AB Wizard in the Leica LAS AF software.

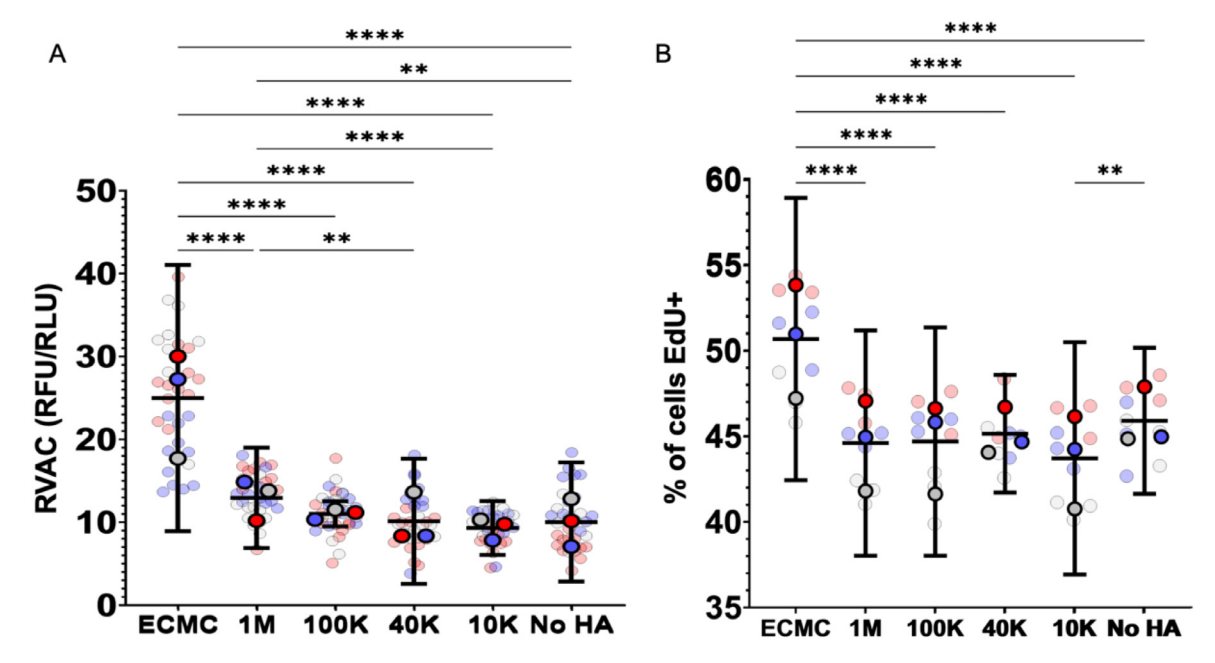


Fig. 1. Soluble 1M HA increases viability, but soluble HA does not affect proliferation. Human cerebral microvascular endothelial cells (HCMVECs) were treated with 1 mg/ml HA with MW ranges of 750-1000 kDa (1M), 100-150 kDa (10K), 41-65 kDa (40K), or 10-20 kDa (10K). As a positive control, HCMVECs were cultured in endothelial cell media complete with an endothelial cell growth supplement (ECMC) or endothelial cell media without the growth supplement or HA (No HA). Cell health was characterized by the ratio of viable to apoptotic cells (RVAC) (A) and proliferation (B). Data points shown in 1A include at least 10 treatment replicates and 3 experimental replicates (n=33 for ECMC, 40K, and 10K, n=34 for 1M, n=35 for 100K, and n=32 for No HA). Data shown in 1B include 3 treatment replicates and 3 experimental replicates (n=9 for each conditions). Data are reported as SuperPlots showing the mean with 95% confidence interval (CI) of the experimental replicates with individual treatment replicate points. Experimental replicates are distinguished by color. *p<0.05. *p<0.01. ***p<0.001. ****p<0.0001.

2.16. Transfection and TIRF microscope observations

HCMVECs were transfected with 1 µg of CD44-Halo7 plasmid DNA by electroporation (Gene Pulser XCell, BioRad). Tranfected cells were seeded on Applied Cell Extracellular Matrix coated glass-bottom dishes (Iwaki) and cultured for 16 h. Cells were labeled with 50 nM HaloTag-TMR (Promega) at 37°C for 20 min and washed three times with fresh medium before observation. TIRF microscope observation was performed at 37°C in culture medium within a stage top incubator (Tokai Hit). TIRF microscope (Eclipse Ti2, Nikon) equipped with 100x, 1.49 numerical aperture objective, 561-nm diode laser and iXon Ultra EMCCD camera (ANDOR) was used for single-molecule imaging. The videos were acquired 30 frames per second. Coordinate determination and trajectory tracking were performed by a C++ based computer program developed by Dr. Akihiro Kusumi's group [66-68]. After generating meansquare displacement versus time increment (MSD- Δt) plot for each trajectory, diffusion coefficient was calculated by liner fit of the time window where the time increment = 2 to 4.

2.17. Statistical methods

All statistical analysis was performed using GraphPad Prism 9.5.1. For clarity, *in vitro* experiments will use the following replicate hierarchy: biological replicates refer to the number of cell lines, experimental replicates refer to each run of an experiment, treatment replicates refer to each separate well of cells receiving treatment as these wells are dynamic since there are live cells and thus are different samples, and technical replicates refer to multiple measurements of the same sample. Replicate numbers are noted in figure legends. All data from *in vitro* experiments, with the exception of Figs. 7 and 8 due to large numbers of treatment replicates, are shown as SuperPlots [87] where the individual treatment replicate points are shown and overlaid with a scatter plot of the means for each experimental replicate as well as a line and bar representing the mean with 95% CI unless other-

wise noted in the figure legend. Two-way ANOVA and post-hoc Tukey's multiple comparisons test were performed to calculate statistical significance in Fig. 1 (Sections 2.2 and 2.3), 2 (Section 2.4), 3 (Sections 2.2 and 2.3), 6 (Section 2.3), and S2 (Section 2.4). A nested t-test was performed to calculate statistical significance in Fig. 5 (Section 2.12). A Kruskal-Wallis and Dunn's multiple comparisons test were performed to calculate statistical significance in Fig. 7 (Section 2.16) and 8 (Section 2.17).

3. Results and discussion

3.1. Effects of HA molecular weight on HCMVEC behavior

3.1.1. Molecular weight of solubilized HA affects HCMVEC viability, but not proliferation

We characterized the effects of HA MW on HCMVEC viability. apoptosis, and proliferation 24 h after addition of 1 mg/ml HA of varying MW (750-1000 kDa (1M HA), 100-150 kDa (100K), 41-65 kDa (40K), and 10-20 kDa (10K)) into the culture media. For assessment of viability and apoptosis, a Promega ApoLive-GloTM Multiplex Assay was used to measure the ratio of viable-to-apoptotic cells (RVAC) in each well (Fig. 1A). Results indicate a trend where RVAC was higher with exposure to HMW HA. As a positive control, HCMVECs were cultured in EC media complete (ECMC), which contains additional growth factors that promote cell survival and proliferation, as evidenced by the higher RVAC. Of the experimental conditions, 1M HA promoted a statistically significant (p < 0.05) increase in RVAC compared to 40K, 10K, and No HA conditions. This increase in cell RVAC does not appear to be caused by differences in proliferation, as the percentages of cells which had proliferated during the 2-hour pulse with EdU (22 h after initial addition of HA treatment) was not statistically significant different across any HA conditions (Fig. 1B). Together, these data suggest a possible protective role for HMW HA in the brain microvasculature, where HMW HA inhibits HCMVEC apoptosis and may act to maintain homeostasis.

J. Karam, B.J. Singer, H. Miwa et al. Acta Biomaterialia 169 (2023) 228-242

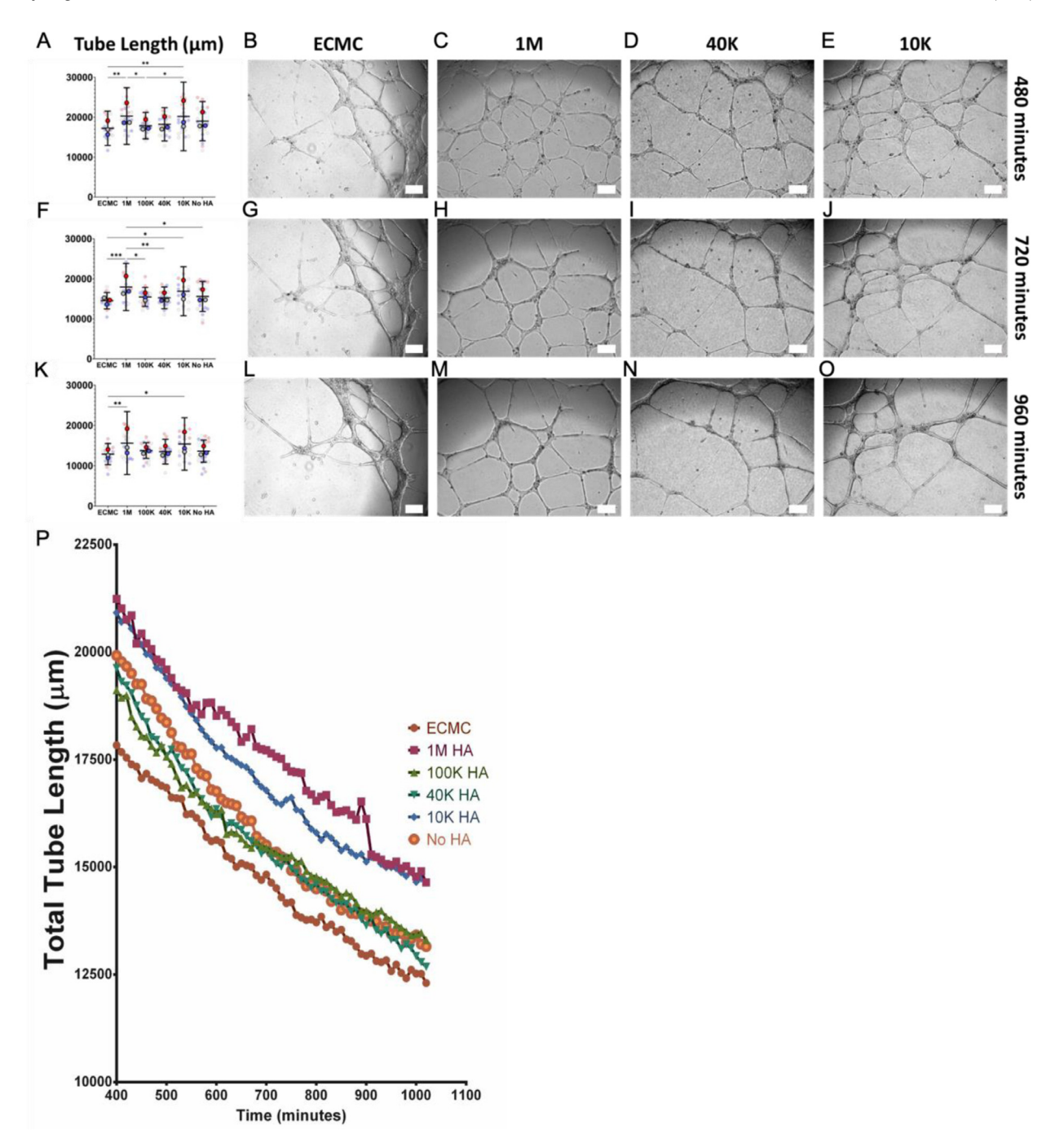


Fig. 2. 1M and 10K HA promote more stable tube formation. For all conditions n=21 wells with 7 treatment replicates and 3 experimental replicates repeats (distinguished by different colors). Bar graphs plotting total tube length and representative images were chosen for ECMC, 1M, 40K, and 10K at 480 min (A-E), 720 min (F-J), and 960 min (K-O). Two-way ANOVA and Tukey's multiple comparisons tests were performed on the total tube length to test for statistical significance at individual time points. Data are reported as SuperPlots showing the mean with 95% confidence interval (CI) of the experimental replicates with individual treatment replicate points. Experimental replicates are distinguished by color. Fig P shows total tube length over time for all conditions. *p<0.05. **p<0.001. ****p<0.001. ****p<0.0001. Scale bars = 200 μm.

3.1.2. 1M HA promotes more stable tube formation in HCMVECs

Using a GeltrexTM tube formation assay and time lapse microscopy, we tracked HCMVEC angiogenesis by measuring the total tube length, defined as the straight-line length of all tubular structures in an image (Fig. 2). The data indicate that 1M HA or 10K HA, but not 100K or 40K HA, promotes stability of newly formed, HCMVEC tube structures (Fig. 2). A two-way ANOVA found that time (F=510.42) and HA molecular weight (F=3.55), as well as the interaction between the two factors (F=1.49), all had statistically significant effects on total tube length. While there is a visual trend towards longer tube lengths over 400 to 1020 min for both the 1M HA and 10K HA conditions (Fig. 2P), interroga-

tion of specific time points (8, 12, and 16 h) using Tukey's multiple comparisons tests. At 480 min, or 8 h, cells treated with 1M HA or 10K HA had significantly higher average total tube length compared to ECMC and 100K HA. (Fig. 2A–E). At 720 min, or 12 h, only 1M HA-treated cells had significantly larger total tube lengths compared to all conditions except 10K HA, which was only significantly longer than ECMC (Fig. 2F–J). Last, at 960 min, or 16 h, the differences between conditions begin to lessen as the tubes disintegrate, an expected occurrence in this type of assay as there are no pericytes or smooth muscle cells to stabilize the newly formed tubes [69]. At 16 h, both the 1M HA and 10K conditions had significantly larger total tube lengths than the ECMC condition (Fig. 2K–

O). The ECMC conditions consistently supported the shortest total tube length, even compared to the "No HA" condition, suggesting that removing the EC growth supplement, the differential component of the ECMC condition, from the media increases tube formation. This is not unexpected, given that the growth supplement is designed to support EC proliferation, not tube formation, and thus, includes several growth factor mitogens. While branching is often considered a sign of active angiogenesis, no significant differences in the number of branches across conditions or over time were observed (Fig. S2G).

Overall, our data suggest that 1M HA and 10K HA stimulate greater tube formation than either 100K HA or 40K HA in HCMVECs. Previous studies have also found that LMW HA (<10 kDa) stimulates formation of longer tubes of rat aortic ECs [22] and HUVECs [19]. However, there was no evidence in our studies that LMW HA stimulated HCMVEC proliferation or migration (Fig. S1) and, thus, this does not appear to be the cause for increased total tube length in angiogenesis assays, as has been widely speculated [19,22,70]. In contrast to at least one previous study [22], we find that HMW (1M HA) treatment resulted in higher total tube lengths maintained over a longer time period. The scope of this study did not measure hyaluronidase activity or the molecular weight distribution of degraded HA fragments in the culture media and thus, future studies will be required to explore whether 1M HA was more readily degraded into pro-angiogenic, 10K HA fragments than were the 40K HA and 100K HA, and/or if hyaluronidase production was increased in the presence of 1M HA.

3.2. Effects of HA MW on the angiogenic potential of HMAPS

3.2.1. Microfluidic generation of HMAPS with low storage modulus

MAP scaffolds are a recent advance in the field of biomaterials that are able to combine injectability with precise control over porosity to promote wound healing [61,62,71-73]. To form HMAPS, HA was modified to include thiol groups to enable crosslinking of individual hydrogel microparticles and subsequent annealing of crosslinked microparticles, as detailed in the Experimental Methods section. Thiolated HA (HA-SH) and vinyl sulfone-terminated 4-arm poly(ethylene)-glycol (PEG-VS) modified with RGD and Flamma 552-SH were injected into a flow-focusing microfluidic device [71] to form microparticles with an excess of thiol to enable annealing of microparticles (Fig. S3A). The degree of thiolation of HA varied depending on MW due to differences in chain length requiring increased modification in lower molecular weights to enable crosslinking (Table S1). Bulk hydrogels made with the same formulations as the microparticles were used to assess rheological properties, which were assumed to be the same in bulk gels and microparticles, at least at the size scale of a cell. All hydrogel formulations were designed to have a microparticle storage modulus between 100 and 200 Pa, in the range of native brain tissue where HCMVECs reside [74] (Fig. S3B). Given that 1M HA and 40K HA in soluble form elicited the most differential responses from HCMVECS (Figs. 1 and 2) and that no statistically significant differences in storage modulus were observed in microparticles made from 1M HA or 40K HA, investigations using 3D, annealed HMAPS experiments were restricted to these conditions. Further, when swollen in physiological buffer, there were no significant differences between the mean particle diameters of the two HMAPS conditions (Fig. S3C). As multiple previously published reports have established a direct relationship between diameter of spherical microparticles and median pore size when annealed into scaffolds [61,62,71,75,76], HMAPS from 40K HA and 1M HA microparticles are expected to be comparable. Based on one such previous study, we expect that our spherical microparticles will anneal into scaffolds with a median pore size around 40 µm [71].

3.2.2. 1M HA HMAPS support HCMVEC viability, but not proliferation, better than 40K HA HMAPS

Data shown in Fig. 1 suggests that 1M HA, but not 100K, 40K, or 10K HA, is protective for HCMVECs because it significantly increased cell viability without any effects on proliferation. This trend persisted in 3D cultures, where HCMVECs cultured in 1M HA HMAPS exhibited significantly higher RVAC than those cultured in 40K HA HMAPS (Fig. 3A). As with soluble HA treatment (Fig. 1B), there were no effects of HA molecular weight on proliferation when HA was chemically modified and crosslinked (Fig. 3A). Together, these findings suggest that 1M HA maintains a protective role after chemical modification (<10%) and subsequent crosslinking. It has been reported previously that increasing modification of HA interferes with HA-CD44 binding [7,77]. Thus, future studies would benefit from investigating how this interference of HA-CD44 interactions affects the bioactivity of crosslinked HA.

3.2.3. Crosslinked 1M HA, but not 40K HA, facilitates angiogenic activity in vitro

Promoting adequate vascularization after implantation of a biomaterial can greatly improve wound healing [39,78,79], even with complex trauma pathologies such as after spinal cord injury [80-82]. The trends shown in Fig. 2, which suggest that soluble 1M HA promotes more stable tube formation in GeltrexTM cultures than do smaller HA fragments, persisted when culturing HCMVECs with crosslinked HA cultured in 3D HMAPS. After 48 h, HCMVECs cultured in 1M HA HMAPS (compared to 40K HMAPS cultures) qualitatively exhibited greater branching and interconnectedness of multi-nucleated, vessel-like structures extending throughout the 3D network created by annealed microparticles (Fig. 4). In 40K HA HMAPS, HCMVECs did not form obvious vessel-like structures with branching and remained primarily on the scaffold surface where initially seeded, rather than penetrating scaffolds in three dimensions. Compared to HCMVECs seeded onto 40K HA HMAPS, treatment of cells seeded onto GeltrexTM with soluble 40K HA (Fig. 2D, 2I, 2N) appears to better support formation of vessel-like structures. Given this result and that LMW HA is typically present in vivo as fragments from a degraded HMW HA matrix [27,38,83], it is possible that crosslinking LMW HA impedes its ability to stimulate angiogenic behavior. It is also possible that either thiolation or crosslinking hinders binding and activation of CD44 receptors. Kwon et al. reported that raising the degree of modification from 10% to 20% was reduce HA-CD44 binding efficiency, and modification of more than ${\sim}40\%$ of disaccharides on ${\sim}75{\text{--}135}$ kDa HA prevents most CD44 binding [7]. As a minimum of 4 HA disaccharide units (\sim 1.6 kDa) is needed to bind CD44 [6], it is reasonable to expect, compared to the higher molecular weight HA used in these previous reports, that the same degree of modification of the smaller, 40K HA used here (41-65 kDa) would have fewer binding sites for CD44 and, thus, bind CD44 less efficiently. A loss of CD44 binding activity may explain why 40K HA, modified at \sim 15%, exhibits a reduced ability to induce tube formation than soluble, unmodified 40K HA or crosslinked, modified 1M HA. Interestingly, Qazi et al. showed extensive endothelial cell sprouting and vessellike formation in HMAPS made with 60 kDa HA, modified at \sim 14%, in in vitro HUVEC cultures [75]. HUVECs are more migratory, proliferation, and form more tube-like structures in the presence of soluble LMW HA [19,46], in agreement with the Qazi et al. study which used insoluble, LMW HA HMAPS [75]. This supports our presented results as HMW HA supports HCMVEC tube-like formation in soluble and crosslinked forms, just as LMW HA supports HUVEC tube-like formation in soluble and crosslinked forms with relatively similar modification levels. These results strengthen the need for interrogating the HA molecular weight-dependent bioactivity in HA-based biomaterials using a wide variety of cell types and modification levels.

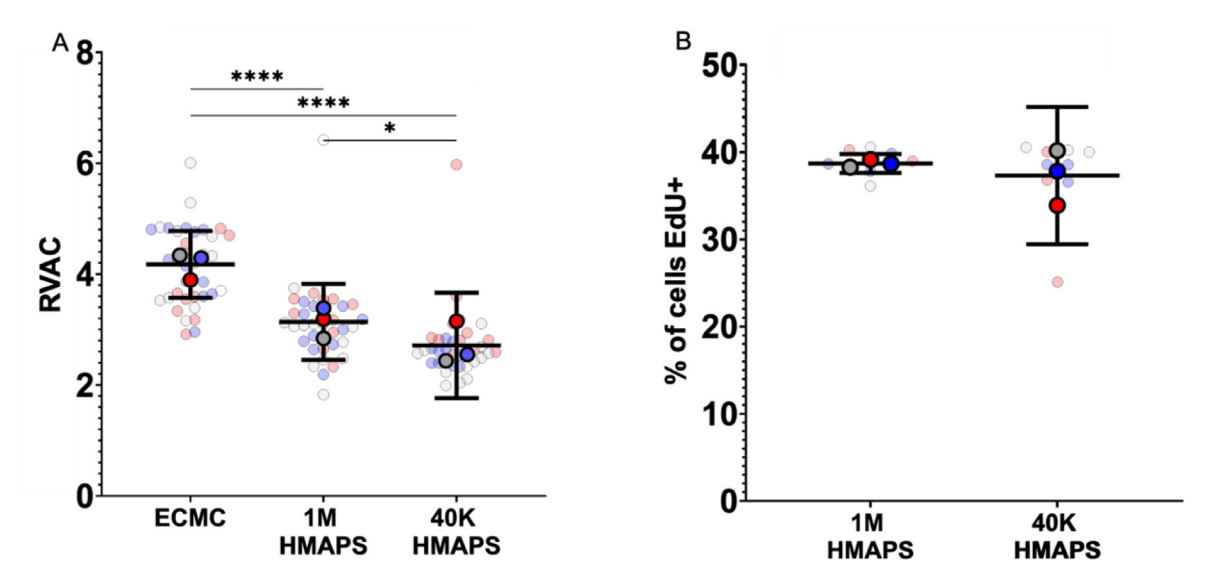


Fig. 3. HMAPS of 1M HA, compared to those of 40K HA, improve cell viability, but have no effect on proliferation. Human cerebral microvascular endothelial cells (HCMVECs) were cultured in HMAPS made with 1M HA (1M 3D) and HMAPS made with 40K HA (40K 3D). Cell health was characterized by the ratio of viable to apoptotic cells (RVAC) (A) and proliferation (B). Given the increased cell number required for 3D cultures, the gains had to be reduced for fluorescent and luminescent readings and thus HCMVECs were cultured in 2D with ECMC as a positive control for the ApoLive-GloTM assay. Data shown in 3A include 12 treatment replicates and 3 experimental replicates. Data shown in 3B include 3 treatment replicates and 3 experimental replicates. Data are reported as SuperPlots showing the mean with 95% confidence interval (CI) of the experimental replicates with individual treatment replicate points. Experimental replicates are distinguished by color. * *p <0.001. * *p <0.0

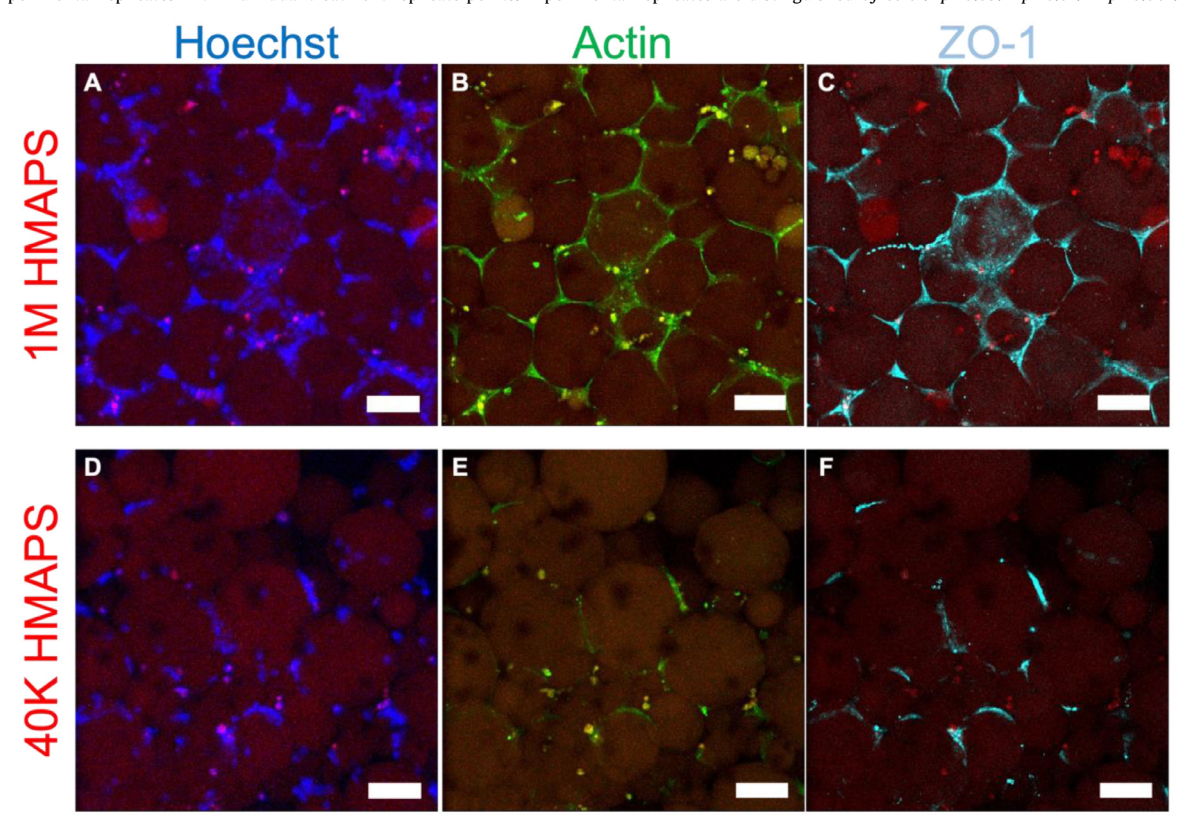


Fig. 4. HMAPS of 1M HA, compared to those of 40K HA, promote more multinucleated vessel-like formation *in vitro*. Human cerebral microvascular endothelial cells (HCMVECs) were cultured in HMAPS made with 1M HA (1M 3D) and 40K HA (40K 3D). After 48 h, cultures were fixed, permeabilized, and stained for actin (B, E) and the tight junction protein, ZO-1 (C and F). Hoescht was used as counter-stain to label nuclei (A and D). HMAPS can be seen in red in the images. Images are representative max projections of z-stacks with slices 2 μm apart in the middle of the scaffolds. Scale bars = 100 μm.

3.2.4. Crosslinked 1M HA, but not 40K HA, facilitates vascularization of HMAPS implants

HMAPS-forming microparticles were injected subcutaneously and allowed to anneal *in situ* in mice. After 9 days, implants and surrounding tissue were explanted, fixed, sectioned, and immunostained to visualize blood vessels, using a laminin antibody, nuclei, and the CD44 receptor. Fig. 5 shows representative images of tissue

sections from the center of the implant. From each animal (N=3 biological repeats), immunofluorescence signals from 2-3 sections per implant condition (1M HMAPS or 40K HMAPS), representative of scaffold implant centers, were quantified by first selecting a region-of-interest (ROI) to isolate the biomaterial from the peripheral muscle and fat. All sections from each animal were averaged together for statistical calculations using a nested t-test.

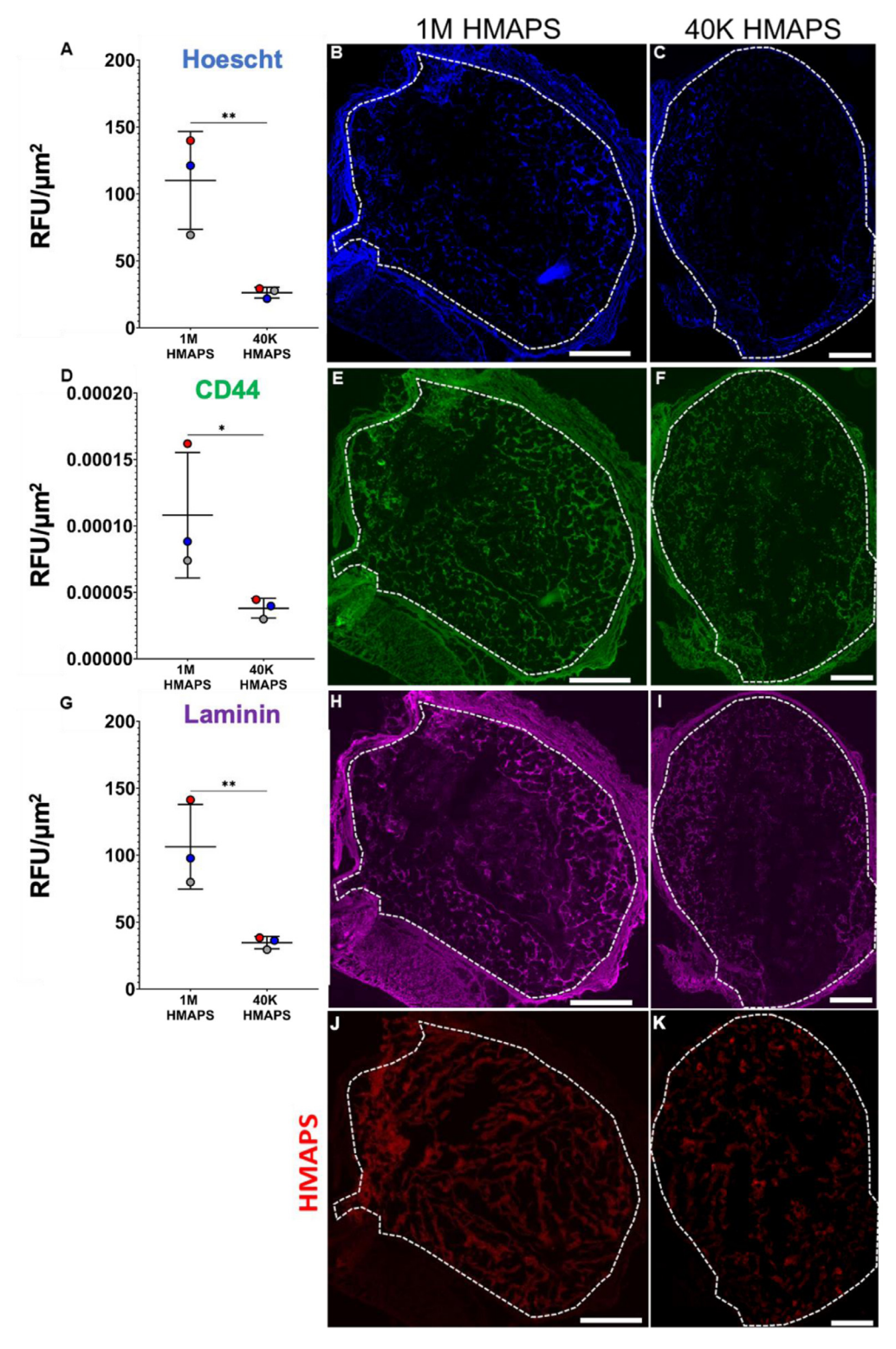


Fig. 5. Crosslinked 1M HA promotes greater vessel formation in vivo. HMAPS were injected subcutaneously in mice. After 9 days, injections were explanted and stained for Hoescht (nuclei, A-C), laminin CD44 (D-F) and Laminin (blood vessels, G-I). Images were quantified by measuring the sum of the fluorescent intensity inside the injection site ROI (white dashed lines) and normalizing to the area of the ROI (A,D,G). Data is reported as the ratio of relative fluorescent units (RFU) to area of the ROI (μ m²) using raw data showing the mean with standard deviation. At least 2 sections (technical replicates) were used from 3 separate animals (biological replicates) for quantification. A nested t-test was used to calculate statistical significance. Representative images of nuclei (B, C), CD44 (D, E), Laminin (H, I), and HMAPS (J, K) are shown. Brightness was enhanced to increase visibility of images. Scale bars = 1000 μ m. *p<0.05. *p<0.01.

J. Karam, B.J. Singer, H. Miwa et al. Acta Biomaterialia 169 (2023) 228-242

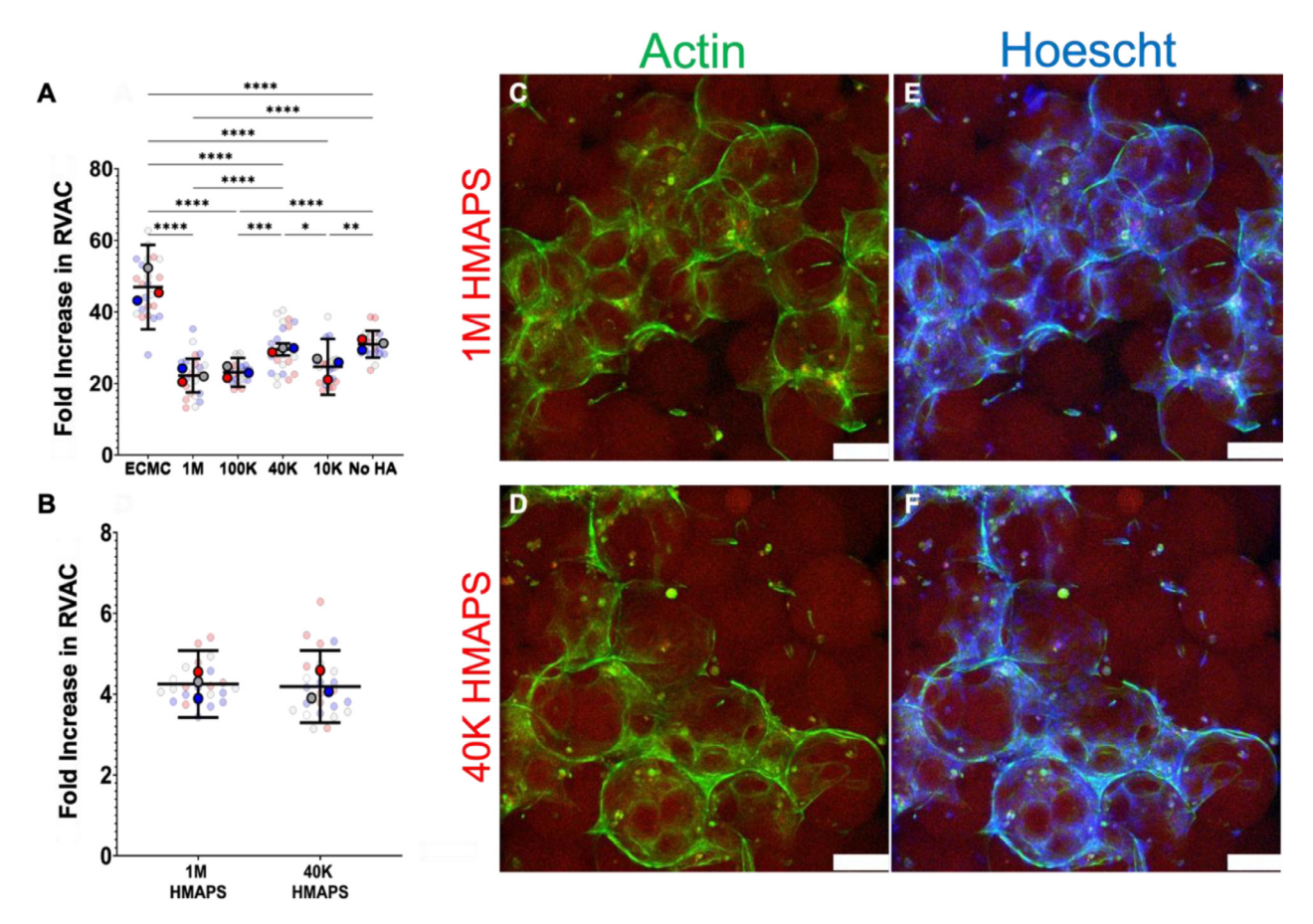


Fig. 6. Clustering of CD44 increases viability and tube formation in all HA MW conditions. Antibody-mediated clustering of CD44 was performed on HCMVECs, which were then cultured in 2D and treated with solubilized 1 mg/ml HA (A) or in HMAPS (B) made with 1M HA (1M 3D) and HMAPS made with 40K HA (40K 3D). The fold increase in RVAC after CD44 clustering of soluble HA (A) and crosslinked HA (B) cultures was measured after 24 and 48 h, respectively. Data are reported as SuperPlots showing the mean with 95% confidence interval (Cl) of the experimental replicates with individual treatment replicate points. Experimental replicates are distinguished by color. After 48 h, 3D crosslinked HA HMAPS cultures were fixed, permeabilized, and stained for actin (C and D). Hoescht was used as counter-stain to label nuclei (E and F). Images are representative max projections of z-stacks with slices 2 μ m apart. Scale bar is 100 μ m. *p < 0.05. **p < 0.01. ****p < 0.001. ****p < 0.0001. ****p < 0.0001.

Within the ROI, a fluorescence intensity sum was measured to give relative fluorescence units (RFU) and then normalized by the ROI area. Data show that significantly more cells (Fig. 5A-5C) infiltrated 1M HMAPS implants than 40K HMAPS. In addition, cells infiltrating 1M HA HMAPS had significantly higher expression of CD44 (Fig. 5D-5F) and laminin (Fig. 5G-5I). Laminin immunostaining corresponded to vessel-like features in the 1M HMAPS, which were not apparent in the 40K HMAPS. This result agrees with in vitro results shown in Figs. 2 and 4. Additionally, 9 days after implantation, both 1M and 40K HMAPS were retained at the site of injection and remained relatively intact (Fig. 5] and 5K). Overall, HMAPS fabricated from 1M HA facilitated greater scaffold formation of multinucleated vessel-like structures, perhaps because of more efficient CD44 interactions, recruitment of ECs by degraded LMW HA fragments, and/or stabilization of early tubules by HMW HA.

3.3. CD44 clustering plays a role in the MW-dependent bioactivity of HA

3.3.1. Forced CD44 clustering increases HCMVEC survival and promotes angiogenesis independently of the MW of HA provided

It has been long hypothesized that the MW-dependent bioactivity of HA involves CD44 receptors [4,17,49,50,84], which cluster in response to HMW HA, but not LMW HA [49,50,84]. Although CD44 clustering has not been widely studied, it has been shown to directly affect the Hippo signaling pathway [49]. While there is still much to learn about CD44-Hippo interactions, down-

stream YAP/TAZ regulates cell-density dependent growth. CD44 clustering-induced activation of Hippo inactivates YAP/TAZ which then accumulate in the cytoplasm promoting quiescence [49]. It is possible this could be an underlying mechanism behind why HMW HA promotes increased RVAC compared to LMW HA. To test the HMW HA-induced CD44 clustering hypothesis, we used a previously published method of antibody-mediated crosslinking of CD44 to induce clustering [49]. HCMVECs were pretreated with the crosslinking antibody prior to seeding on either tissue-culture plastic or HMAPS (made from either 1M or 40K HA). For cells on tissue-culture plastic, soluble HA of varying molecular weights was added to the culture media. Viability was assessed at either 24 h (2D cultures, Fig. 6A) or 48 h (HMAPS cultures, Fig. 6B) after seeding to match previous experiments. Antibody-treated HCMVECs in 2D culture were then treated with soluble HA of varying MWs. In all conditions, antibody-induced CD44 clustering increased RVAC and, thus, data are reported as fold increase over cultures without crosslinking antibody. Compared to HCMVECs cultured with ECMC, 1M HA, or 100K HA, the LMW HA conditions (40K, 10K) and "No HA" control showed greater increases in viability over matched cultures without antibody pretreatment. This trend was conserved for HCMVECs seeded in HMAPS, where antibody-mediated CD44 crosslinking increased RVAC more in the 40K HA condition than in the 1M HA condition. These data indicate that CD44 clustering increases RVAC in HCMVECs, supporting the hypothesis that HMW HA-induced CD44 clustering, which would be present in the baseline/no antibody condition, increases cell viability.

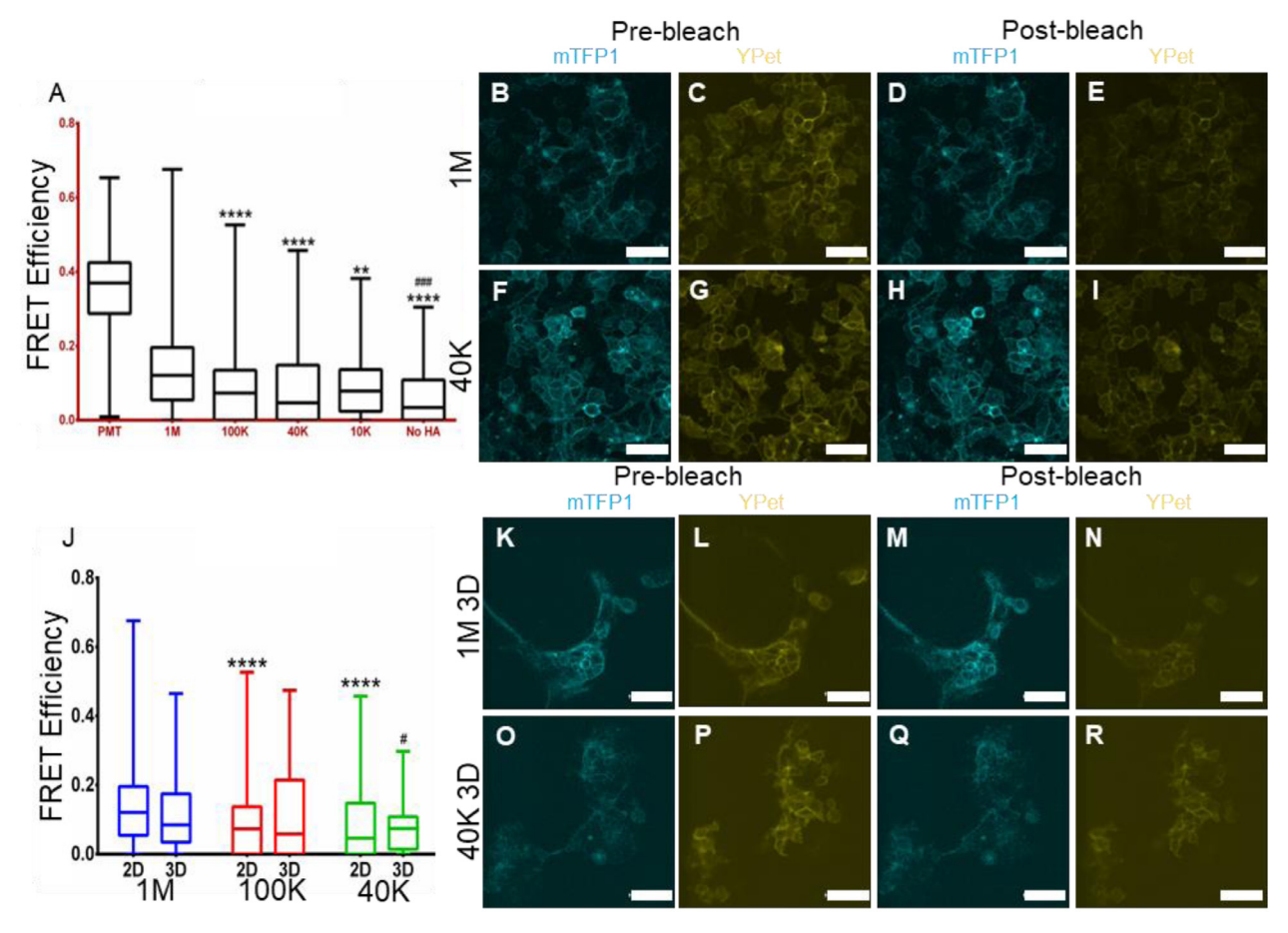


Fig. 7. CD44 clustering increases as HA MW increases. To determine CD44 clustering in response to soluble HA MW, acceptor-photobleaching FRET was performed (A-I). For PMT, 1M, 100K, 40K, 10K, and no HA conditions n=160, 226, 216, 211, 204, and 187 cells, respectively. The 63x high-magnification pre-bleach (B, C, F, G) and post-bleach (D, E, H, I) images of mTFP1 and Ypet are shown. Acceptor-photobleaching FRET was also performed in 3D crosslinked HA HMAPS cultures made with 1M, 100K, and 40K HA (J-R). The 63x high-magnification pre-bleach (K, L, O, P) and post-bleach (M, N, Q, R) images of mTFP1 and Ypet are shown. Scale bar is 50 μ m. **p<0.01 vs 1M. ****p<0.001 vs 1M or 1M 2D. #p<0.05 vs 1M 3D. ###p<0.001 vs 10K.

We then evaluated how antibody-induced CD44 clustering affected angiogenic activity in HMAPS cultures. Representative images showing maximum intensity projection of confocal z-stacks of fluorescent actin fibers are provided in (Fig. 6 C-F). Qualitatively, cells in 40K HA HMAPS with antibody-mediated CD44 crosslinking developed interconnected, branched networks comparable to cells seeded in 1M HA HMAPS with or without antibody treatment. Together, these data suggest that CD44 clustering can induce angiogenic behavior and that the HMW HA may induce differential effects on ECs through more efficient CD44 clustering.

3.3.2. CD44 clustering increases with increasing HA MW

To evaluate the effects of HA MW on CD44 clustering, a model cell line, Lenti-XTM 293T, was transduced with a lentivirus to overexpress fluorescently tagged CD44 at the plasma membrane. Specifically, CD44-mTFP1 and CD44-YPet were overexpressed in single cultures and mTFP1 and YPET used as an acceptor-donor pair, where fluorescence resonance energy transfer (FRET) only occurs when a mTFP1 and YPET receptor are within 6 nm of each other. When FRET transfer occurs, the CD44 receptors are considered to be "clustered." Using an accepter-photobleaching FRET method [50] in these model cells, we were able to measure the extent of CD44 clustering in the presence of HA polysaccharides with varying molecular weights (Fig. 7). FRET measurements were acquired after treatment of transduced HEKs with solubilized HA for 2 h. Lenti-XTM 293T cells overexpressing a mTFP1-YPet fusion protein with a plasma membrane targeting (PMT) were included

as a positive control (denoted as "PMT control") representing the maximum possible FRET efficiency. In the PMT control construct, mTFP1 and YPET were joined by a flexible linker approximately 16 nm long when fully extended. Because the linker is larger than the 6 nm Förster radius for the mTFP1-YPet FRET pair [85], the typical FRET efficiency observed for the PMT control was around 40 reflecting a situation where the linker was only in a conformation state enabling FRET less than half the time.

While a similar FRET approach has been used previously to investigate CD44 clustering in response to varying HA molecular weight in a model cell line [50], the present studies expanded investigation to explore effects of a larger range of HA molecular weights. In 2D cultures, FRET efficiency, and therefore the extent of CD44 clustering, was significantly higher with exposure to 1M HA than HA polysaccharides of lower molecular weights (Fig. 7A-I). This result further supports the hypothesis that HMW HA more efficiently clusters CD44 than does LMW HA. While not statistically significant, the median FRET efficiency in the 10K HA condition was trended higher than the median efficiencies for the 10K and 40K conditions, possibly indicating that 10K HA was able to cluster HA more efficiently than the mid-range polysaccharides. Thus, it is possible that CD44 clustering mediates the angiogenic effects of 10K HA or 1M HA, but not 40K HA or 100K HA, as shown in Fig. 2. We next explored how chemical modification and subsequent crosslinking of HA affects its ability to cluster CD44 using 3D HMAPS cultures. As with the soluble HA experiments, 1M HA HMAPS cultures showed significantly higher FRET efficiencies com-

Acta Biomaterialia 169 (2023) 228–242

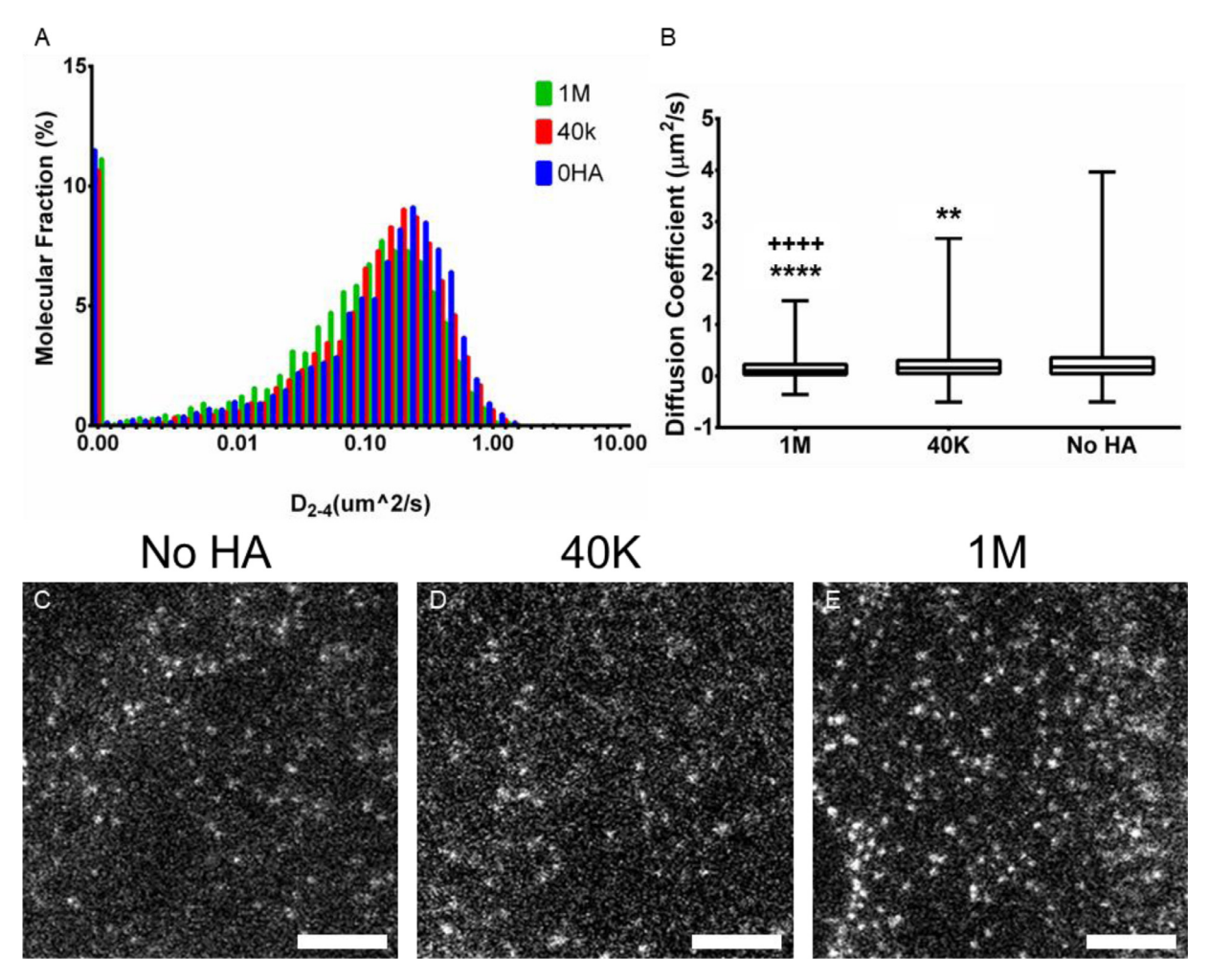


Fig. 8. Diffusion of CD44 through the cell membrane increases as HA MW decreases. To determine CD44 receptor kinetics, single molecule tracking was performed using TIRF microscopy in response to 1M, 40K, and No HA. The molecular fraction distribution of diffusion coefficients (A) and min to max box plot of diffusion coefficients (B) show CD44 diffusion increases as HA MW decreases. A Kruskal-Wallis and Dunn's multiple comparisons test show that 1M HA slows CD44 diffusion significantly compared to 40K and No HA conditions. Representative TIRF images are shown (C-E). Scale bar is 5 μ m. **p<0.001 vs No HA. ****p<0.0001 vs No HA. ++++p<0.0001 vs 40K.

pared to 40K HA HMAPS or 100K HMAPS cultures (Fig. 7J–R). Together, data shown in Figs. 2, 4, and 5–7 indicate that both 1M HA and 10K HA promote angiogenesis, likely through increased CD44 clustering, and that 10% modification and crosslinking of 1M HA does not hinder this ability.

3.3.3. Diffusion of CD44 receptors increases with decreasing HA molecular weight

Finally, total internal reflection fluorescence (TIRF) microscopy was used to visualize real-time CD44 receptor kinetics in live HCMVECs in response to HA (Fig. 8). The diffusion coefficient was calculated for HCMVECs transfected to express HaloTag-labeled CD44, cultured with soluble 1M HA, 40K HA, or No HA, and TIRF for single-molecule tracking of CD44 receptors. A histogram showing the molecular fraction of CD44 receptors with a particular diffusion coefficient suggests that larger HA polysaccharides act to slow diffusion of at least some CD44 receptors (Fig. 8A). Comparing the median diffusion coefficients for CD44 in each condition, we report that addition of 1M HA significantly (p <0 .0001) decreased CD44 diffusion compared to 40K HA and negative control ("No HA") conditions (Fig. 8B). Addition of 40K HA also significantly decreased CD44 diffusion compared to the negative control (p < 0.01), yet to a lesser extent than 1M HA (Fig. 8B). In sum, HA binding to CD44 decreases receptor mobility in the cell membrane and that higher molecular weight HA decreases mobility to a greater extent. This observation suggests that the number of CD44 receptors bound per HA molecule, or multivalency, increases with HA molecular weight [86]. While decreased receptor mobility could indicate increased receptor clustering, we were not able to observe CD44 clustering in HCMVECs using TIRF single-molecule imaging. We suspect that CD44 in HCMVECs is expressed and /or clustered at levels below our detection ability.

While our FRET measurements and WB studies in other papers do indicate that clustering occurs, it could possibly be 'loose' where several receptors are brought together on a single lipid raft [86]. This further supports our hypothesis that CD44 clustering may mediate the MW-dependent bioactivity of HA. By slowing down diffusion of CD44 in the membrane, the likelihood of clustering should increase. However, visualizing CD44 clustering in wild type cells has proven difficult for the field as only one study has shown HA-induced CD44 clustering in human wild type cells, specifically in human adipose-derived stem cells [84]. Until that obstacle can be overcome, it is likely that indirect, supportive evidence such as the data presented in this report will be all that can be shown in investigating this mechanism.

4. Conclusion

In this study, we aimed to understand how the MW of HA affects the angiogenic potential of HA-based biomaterials for wound

J. Karam, B.J. Singer, H. Miwa et al. Acta Biomaterialia 169 (2023) 228–242

healing. HA has a very well-documented MW-dependent bioactivity [12,19,20,22,23,25,49,50,84]. We showed that soluble and crosslinked 1M HA exhibited a greater RVAC in HCMVECs without increasing proliferation compared to lower HA MWs, suggesting that 1M HA possibly has a protective effect as it is able to form a PCM, while LMW HA cannot. We also showed that soluble 1M and 10K HA promote greater tube stability than 100K and 40K HA. This trend was conserved when investigating vessel formation in HCMVECs cultured in HMAPS made with crosslinked 1M and 40K HA. 1M HMAPS promoted greater multinucleated vessellike structure formation than 40K HMAPS both in vitro and in vivo. We hypothesized that CD44 clustering may mediate the MWdependent bioactivity of HA. We first used an antibody-mediated crosslinking method to force CD44 clustering, which resulted in increased RVAC and multinucleated vessel-like structure formation in HCMVECs regardless of HA MW or crosslinking. We then used a model HEK293T cell line to overexpress CD44 with a mTFP1-YPet FRET pair. We showed here that soluble 1M and 10K HA promote higher FRET efficiencies, and thus CD44 clustering, than soluble 100K and 40K HA. We then showed that modifying HA (<20%) and crosslinking into HMAPS does not affect HA-induced CD44 clustering. Last, to further investigate the CD44 clustering mechanism in response to HA MW, we used TIRF microscopy to track single molecule CD44 receptor kinetics showing that CD44 diffusion through the cell membrane significantly decreases as HA MW increases. These data altogether highlight: 1) HA MW is a critical design parameter in the development of HA-based biomaterials, 2) the MW-dependent bioactivity of HA may vary between cell types and HA forms, and 3) CD44 clustering may mediate the MWdependent bioactivity of HA. These three takeaways will inform the future design of HA-based biomaterials for any regenerative application.

Data availability statement

The datasets generated during and/or analysed during the current study are available from the corresponding author on reasonable request.

Declaration of Competing Interest

The authors declare that they have no known competing financial interests or personal relationships that could have appeared to influence the work reported in this paper.

Acknowledgements

Confocal laser scanning microscopy was performed at the California NanoSystems Institute Advanced Light Microscopy/Spectroscopy Shared Resource Facility at the UCLA, supported with funding from NIH-NCRR shared resources (Grant No. CJX1-443835-WS-29646) and NSF Major Research Instrumentation (Grant No. CHE-0722519). In vivo procedures were performed with support from the Division of Laboratory Animal Medicine (DLAM) at the UCLA. TIRF experiment was performed at the Center for Biomedical ResearchSupport Microscopy and Imaging Facility at UT Austin (RRID:SCR_021756). J. Karam was supported by a UCLA Eugene V. Cota-Robles Fellowship. B. Singer and S. Garza were supported by the MARC program. We would like to acknowledge support from a UCLA Henry Samueli School of Engineering and Applied Sciences (HSSEAS) Faculty Research Grant (SKS) and a UCLA Faculty Career Development Award (SKS).

The authors would like to acknowledge funding for this work. S. Seidlits was supported by NSF 1653730 and NIH R01 CA241927-01A1. S. Li was supported by NIH R01GM143485. D. Di Carlo was supported by the Presidential Early Career Award for Scientists

and Engineers (N00014-16-1-2997). H.C. Yeh was supported by NIH EY033106 and NSF 2041345 grants.

Supplementary materials

Supplementary material associated with this article can be found, in the online version, at doi:10.1016/j.actbio.2023.08.001.

References

- [1] K.L. Aya, R. Stern, Hyaluronan in wound healing: rediscovering a major player, Wound Repair Regen. 22 (2014) 579–593.
- [2] R. Stern, A.A. Asari, K.N. Sugahara, Hyaluronan fragments: an information-rich system, Eur. J. Cell Biol. 85 (2006) 699-715.
- [3] M. Litwiniuk, A. Krejner, T. Grzela, Hyaluronic acid in inflammation and tissue regeneration, Wounds 28 (2016) 78–88.
- [4] Z.Z. Khaing, S.K. Seidlits, Hyaluronic acid and neural stem cells: implications for biomaterial design, J. Mater. Chem. B 3 (2015) 7850-7866.
- [5] J.A. Burdick, G.D. Prestwich, Hyaluronic acid hydrogels for biomedical applications, Adv. Mater. 23 (2011) H41–H56.
- [6] S. Banerji, A.J. Wright, M. Noble, D.J. Mahoney, I.D. Campbell, A.J. Day, D.G. Jackson, Structures of the Cd44-hyaluronan complex provide insight into a fundamental carbohydrate-protein interaction, Nat. Struct. Mol. Biol. 14 (2007) 234–239.
- [7] M.Y. Kwon, C. Wang, J.H. Galarraga, E. Puré, L. Han, J.A. Burdick, Influence of hyaluronic acid modification on CD44 binding towards the design of hydrogel biomaterials, Biomaterials 222 (2019) 119451.
- [8] N.H. Attenello, C.S. Maas, Injectable fillers: review of material and properties, Facial Plast. Surg. 31 (2015) 29–34.
- [9] A. Borzacchiello, L. Russo, B.M. Malle, K. Schwach-Abdellaoui, L. Ambrosio, Hyaluronic acid based hydrogels for regenerative medicine applications, Biomed. Res. Int. (2015) (2015) 1–12.
- [10] A. La Gatta, C. Schiraldi, A. Papa, A. D'Agostino, M. Cammarota, A. De Rosa, M. De Rosa, Hyaluronan scaffolds via diglycidyl ether crosslinking: Toward improvements in composition and performance, Carbohydr. Polym. 96 (2013) 536–544.
- [11] S.K. Seidlits, J. Liang, R.D. Bierman, A. Sohrabi, J. Karam, S.M. Holley, C. Cepeda, C.M. Walthers, Peptide-modified, hyaluronic acid-based hydrogels as a 3D culture platform for neural stem/progenitor cell engineering, J. Biomed. Mater. Res. Part A 107 (2019) 704–718.
- [12] Z.Z. Khaing, B.D. Milman, J.E. Vanscoy, S.K. Seidlits, R.J. Grill, C.E. Schmidt, High molecular weight hyaluronic acid limits astrocyte activation and scar formation after spinal cord injury, J. Neural Eng. 8 (2011) 046033.
- [13] S.K. Seidlits, Z.Z. Khaing, R.R. Petersen, J.D. Nickels, J.E. Vanscoy, J.B. Shear, C.E. Schmidt, The effects of hyaluronic acid hydrogels with tunable mechanical properties on neural progenitor cell differentiation, Biomaterials 31 (2010) 3930–3940.
- [14] A.F. Placone, P.M. Mcguiggan, D.E. Bergles, H. Guerrero-Cazares, A. Quiñones-Hinojosa, P.C. Searson, Human astrocytes develop physiological morphology and remain quiescent in a novel 3D matrix, Biomaterials 42 (2015) 134-143.
- [15] E.M. Horn, M. Beaumont, Z.S. Xiao, A. Harvey, G.D. Prestwich, K.M. Horn, A.R. Gibson, M.C. Preul, A. Panitch, Influence of cross-linked hyaluronic acid hydrogels on neurite outgrowth and recovery from spinal cord injury, J. Neurosurg. Spine 6 (2007) 133–140.
- [16] K.A. Scheibner, M.A. Lutz, S. Boodoo, M.J. Fenton, J.D. Powell, M.R. Horton, Hyaluronan fragments act as an endogenous danger signal by engaging TLR2, J. Immunol. 177 (2006) 1272–1281.
- [17] D. Jiang, J. Liang, P.W. Noble, Hyaluronan in tissue injury and repair, Annu. Rev. Cell Dev. Biol. 23 (2007) 435–461.
- [18] D. Jiang, J. Liang, P.W. Noble, Hyaluronan as an immune regulator in human diseases, Physiol. Rev. 91 (2011) 221–264.
- [19] V.B. Lokeshwar, M.G. Selzer, Differences in hyaluronic acid-mediated functions and signaling in arterial, microvessel, and vein-derived human endothelial cells, J. Biol. Chem. 275 (2000) 27641–27649.
- [20] S.A. Back, T.M.F. Tuohy, H. Chen, N. Wallingford, A. Craig, J. Struve, L.L. Ning, F. Banine, Y. Liu, A. Chang, B.D. Trapp, B.F. Bebo, M.S. Rao, L.S. Sherman, Hyaluronan accumulates in demyelinated lesions and inhibits oligodendrocyte progenitor maturation. Nat. Med. 11 (2005) 966–972.
- progenitor maturation, Nat. Med. 11 (2005) 966–972.

 [21] J.E. Rayahin, J.S. Buhrman, Y. Zhang, T.J. Koh, R.A. Gemeinhart, High and low molecular weight hyaluronic acid differentially influence macrophage activation, ACS Biomater. Sci. Eng. 1 (2015) 481–493.
- [22] S. Ibrahim, A. Ramamurthi, Hyaluronic acid cues for functional endothelialization of vascular constructs, J. Tissue Eng. Regen. Med. 2 (2008) 22–32.
- [23] W. Mo, C. Yang, Y. Liu, Y. He, Y. Wang, F. Gao, The influence of hyaluronic acid on vascular endothelial cell proliferation and the relationship with ezrin/merlin expression, Acta Biochim. Biophy. Sin. 43 (2011) 930–939.
- [24] D. Chester, A.C. Brown, The role of biophysical properties of provisional matrix proteins in wound repair, Matrix Biol. 60–61 (2017) 124–140.
- [25] C. De La Motte, J. Nigro, A. Vasanji, H. Rho, S. Kessler, S. Bandyopadhyay, S. Danese, C. Fiocchi, R. Stern, Platelet-derived hyaluronidase 2 cleaves hyaluronan into fragments that trigger monocyte-mediated production of proinflammatory cytokines, Am. J. Pathol. 174 (2009) 2254–2264.

- [26] K.R. Taylor, K. Yamasaki, K.A. Radek, A. Di Nardo, H. Goodarzi, D. Golenbock, B. Beutler, R.L. Gallo, Recognition of hyaluronan released in sterile injury involves a unique receptor complex dependent on toll-like receptor 4, CD44, and MD-2, J. Biol. Chem. 282 (2007) 18265–18275.
- [27] A.D. Gaudet, P.G. Popovich, Extracellular matrix regulation of inflammation in the healthy and injured spinal cord, Exp. Neurol. 258 (2014) 24–35.
- [28] S. Dolma, H. Kumar, Neutrophil, extracellular matrix components, and their interlinked action in promoting secondary pathogenesis after spinal cord injury, Mol. Neurobiol. 58 (2021) 4652–4665.
- [29] A. Avenoso, G. Bruschetta, A. D'Ascola, M. Scuruchi, G. Mandraffino, A. Saitta, S. Campo, G.M. Campo, Hyaluronan fragmentation during inflammatory pathologies: a signal that empowers tissue damage, Mini Rev. Med. Chem. 20 (2019) 54–65.
- [30] G. Abatangelo, V. Vindigni, G. Avruscio, L. Pandis, P. Brun, Hyaluronic acid: redefining its role. Cells 9 (2020) 1743.
- [31] Z.Z. Khaing, A. Ehsanipour, C.P. Hofstetter, S.K. Seidlits, Injectable hydrogels for spinal cord repair: a focus on swelling and intraspinal pressure, Cells Tissues Organs 202 (2016) 67–84.
- [32] L.S. Sherman, S. Matsumoto, W. Su, T. Srivastava, S.A. Back, Hyaluronan synthesis, catabolism, and signaling in neurodegenerative diseases, Int. J. Cell Biol. 2015 (2015) 368584.
- [33] T.L. Adair-Kirk, R.M. Senior, Fragments of extracellular matrix as mediators of inflammation, Int. J. Biochem. Cell Biol. 40 (2008) 1101–1110.
- [34] K.A. Scheibner, M.A. Lutz, S. Boodoo, M.J. Fenton, M.R. Horton, J.D. Powell, M.R. Horton, Hyaluronan fragments act as an endogenous danger signal by engaging TLR2, J. Immunol. 177 (2017) 1272–1281.
- [35] N. Nagy, H.F. Kuipers, P.L. Marshall, E. Wang, G. Kaber, P.L. Bollyky, Hyaluronan in immune dysregulation and autoimmune diseases, Matrix Biol. 78–79 (2019) 292–313.
- [36] A.D. Gaudet, P.G. Popovich, Extracellular matrix regulation of inflammation in the healthy and injured spinal cord, Exp. Neurol. 258 (2014) 24–34.
- [37] M. David-Raoudi, F. Tranchepain, B. Deschrevel, J.C. Vincent, P. Bogdanowicz, K. Boumediene, J.P. Pujol, Differential effects of hyaluronan and its fragments on fibroblasts: Relation to wound healing, Wound Repair Regen. 16 (2008) 274–287
- [38] K.R. Taylor, J.M. Trowbridge, J.A. Rudisill, C.C. Termeer, J.C. Simon, R.L. Gallo, Hyaluronan fragments stimulate endothelial recognition of injury through TLR4, J. Biol. Chem. 279 (2004) 17079–17084.
- [39] E.L. Pardue, S. Ibrahim, A. Ramamurthi, Role of hyaluronan in angiogenesis and its utility to angiogenic tissue engineering, Organogenesis 4 (2008) 203.
 [40] S. Meran, D.W. Thomas, P. Stephens, S. Enoch, J. Martin, R. Steadman,
- [40] S. Meran, D.W. Thomas, P. Stephens, S. Enoch, J. Martin, R. Steadman, A.O. Phillips, Hyaluronan facilitates transforming growth factor-β1- mediated fibroblast proliferation, J. Biol. Chem. 283 (2008) 6530–6545.
- [41] J.W. Austin, C. Gilchrist, M.G. Fehlings, High molecular weight hyaluronan reduces lipopolysaccharide mediated microglial activation, J. Neurochem. 122 (2012) 344–355.
- [42] D.V. Chistyakov, A.A. Astakhova, N.V. Azbukina, S.V. Goriainov, V.V. Chistyakov, M.G. Sergeeva, High and low molecular weight hyaluronic acid differentially influences oxylipins synthesis in course of neuroinflammation, Int. J. Mol. Sci. 20 (2019) 3894.
- [43] A.G. Tavianatou, I. Caon, M. Franchi, Z. Piperigkou, D. Galesso, N.K. Karamanos, Hyaluronan: molecular size-dependent signaling and biological functions in inflammation and cancer, FEBS J. 286 (2019) 2883–2908.
- [44] H. Harada, M. Takahashi, CD44-dependent intracellular and extracellular catabolism of hyaluronic acid by hyaluronidase-1 and -2, J. Biol. Chem. 282 (2007) 5597–5607.
- [45] J. Liang, D. Jiang, J. Griffith, S. Yu, J. Fan, X. Zhao, R. Bucala, P.W. Noble, CD44 Is a negative regulator of acute pulmonary inflammation and lipopolysaccharide-TLR signaling in mouse macrophages, J. Immunol. 178 (2007) 2469–2475.
- [46] Y.Z. Wang, M.L. Cao, Y.W. Liu, Y. Qing He, C.X. Yang, F. Gao, CD44 mediates oligosaccharides of hyaluronan-induced proliferation, tube formation and signal transduction in endothelial cells, Exp. Biol. Med. 236 (2011) 84–90.
- [47] K. Fuchs, A. Hippe, A. Schmaus, B. Homey, J.P. Sleeman, V. Orian-Rousseau, Opposing effects of high-and low-molecular weight hyaluronan on CXCL12-induced CXCR4 signaling depend on CD44, Cell Death Dis. 4 (2013) e819.
- [48] S.M. Ruppert, T.R. Hawn, A. Arrigoni, T.N. Wight, P.L. Bollyky, Tissue integrity signals communicated by highmolecular weight hyaluronan and the resolution of inflammation, Immunol. Res. 58 (2014) 186–192.
- [49] T. Ooki, N. Murata-Kamiya, A. Takahashi-Kanemitsu, W. Wu, M. Hatakeyama, High-molecular-weight hyaluronan is a hippo pathway ligand directing cell density-dependent growth inhibition via PAR1b, Dev. Cell 49 (2019) 590-604.e9.
- [50] C. Yang, M. Cao, H. Liu, Y. He, J. Xu, Y. Du, Y. Liu, W. Wang, L. Cui, J. Hu, F. Gao, The high and low molecular weight forms of hyaluronan have distinct effects on CD44 clustering, J. Biol. Chem. 287 (2012) 43094–43107.
- [51] J.M. Cyphert, C.S. Trempus, S. Garantziotis, Size matters: molecular weight specificity of hyaluronan effects in cell biology, Int. J. Cell Biol. 2015 (2015) 563818
- [52] Y. Luo, F. Liang, X. Wan, S. Liu, L. Fu, J. Mo, X. Meng, Z. Mo, Hyaluronic acid facilitates angiogenesis of endothelial colony forming cell combining with mesenchymal stem cell via CD44/MicroRNA-139-5p pathway, Front. Bioeng. Biotechnol. 10 (2022) 114.
- [53] K.A. Queisser, R.A. Mellema, A.C. Petrey, Hyaluronan and its receptors as regulatory molecules of the endothelial interface, J. Histochem. Cytochem. 69 (2021) 25–34.

- [54] J.B. Leach, K.A. Bivens, C.W. Patrick, C.E. Schmidt, Photocrosslinked hyaluronic acid hydrogels: natural, biodegradable tissue engineering scaffolds, Biotechnol. Bioeng. 82 (2003) 578-589.
- [55] C.E. Schmidt, J.M. Baier, Acellular vascular tissues: natural biomaterials for tissue repair and tissue engineering, Biomaterials 21 (2000) 2215–2231.
- [56] J. Lu, F. Guan, F. Cui, X. Sun, L. Zhao, Y. Wang, X. Wang, Enhanced angiogenesis by the hyaluronic acid hydrogels immobilized with a VEGF mimetic peptide in a traumatic brain injury model in rats, Regen. Biomater. 6 (2019) 325.
- [57] J. Arulmoli, H.J. Wright, D.T.T. Phan, U. Sheth, R.A. Que, G.A. Botten, M. Keating, E.L. Botvinick, M.M. Pathak, T.I. Zarembinski, D.S. Yanni, O.V. Razorenova, C.C.W. Hughes, L.A. Flanagan, Combination scaffolds of salmon fibrin, hyaluronic acid, and laminin for human neural stem cell and vascular tissue engineering. Acta Biomater. 43 (2016) 122–138.
- [58] D. Yee, D. Hanjaya-Putra, V. Bose, E. Luong, S. Gerecht, Hyaluronic acid hydrogels support cord-like structures from endothelial colony-forming cells, Tissue Eng. Part A 17 (2011) 1351.
- [59] M.V. Giraudo, D. Di Francesco, M.C. Catoira, D. Cotella, L. Fusaro, F. Boccafoschi, Angiogenic potential in biological hydrogels, Biomedicines 8 (2020) 436 2020, Vol. 8, Page 436...
- [60] V. Ciccone, M. Zazzetta, L. Morbidelli, Comparison of the effect of two hyaluronic acid preparations on fibroblast and endothelial cell functions related to angiogenesis, Cells 8 (2019) 1479.
- [61] A. Ehsanipour, M. Sathialingam, L.M. Rad, J. De Rutte, R.D. Bierman, J. Liang, W. Xiao, D. Di Carlo, S.K. Seidlits, Injectable, macroporous scaffolds for delivery of therapeutic genes to the injured spinal cord, APL Bioeng. 5 (2021) 16104.
- [62] A. Ehsanipour, T. Nguyen, T. Aboufadel, M. Sathialingam, P. Cox, W. Xiao, C.M. Walthers, S.K. Seidlits, Injectable, hyaluronic acid-based scaffolds with macroporous architecture for gene delivery, Cell. Mol. Bioeng. 12 (2019) 399–413.
- [63] W. Xiao, R. Zhang, A. Sohrabi, A. Ehsanipour, S. Sun, J. Liang, C.M. Walthers, L. Ta, D.A. Nathanson, S.K. Seidlits, Brain-mimetic 3D culture platforms allow investigation of cooperative effects of extracellular matrix features on therapeutic resistance in glioblastoma, Cancer Res. 78 (2018) 1358–1370.
- [64] W. Xiao, A. Ehsanipour, A. Sohrabi, S.K. Seidlits, Hyaluronic-acid based hydrogels for 3-dimensional culture of patient-derived glioblastoma cells, J. Vis. Exp. 2018 (2018) e58176.
- [65] T.A. Tsunoyama, Y. Watanabe, J. Goto, K. Naito, R.S. Kasai, K.G.N. Suzuki, T.K. Fujiwara, A. Kusumi, Super-long single-molecule tracking reveals dynamic-anchorage-induced integrin function, Nat. Chem. Biol. 14 (2018) 497–506 2018 14:5.
- [66] A. Kusumi, T.A. Tsunoyama, K.M. Hirosawa, R.S. Kasai, T.K. Fujiwara, Tracking single molecules at work in living cells, Nat. Chem. Biol. 10 (2014) 524–532 2014 10:7..
- [67] T. Fujiwara, K. Ritchie, H. Murakoshi, K. Jacobson, A. Kusumi, Phospholipids undergo hop diffusion in compartmentalized cell membrane, J. Cell Biol. 157 (2002) 1071.
- [68] P. Sil, N. Mateos, S. Nath, S. Buschow, C. Manzo, K.G.N. Suzuki, T. Fujiwara, A. Kusumi, M.F. Garcia-Parajo, S. Mayor, Dynamic actin-mediated nano-scale clustering of CD44 regulates its meso-scale organization at the plasma membrane, Mol. Biol. Cell 31 (2020) 561–579.
- [69] A.N. Stratman, K.M. Malotte, R.D. Mahan, M.J. Davis, G.E. Davis, Pericyte recruitment during vasculogenic tube assembly stimulates endothelial basement membrane matrix formation, Blood 114 (2009) 5091–5101.
- [70] D.C. West, I.N. Hampson, F. Arnold, S. Kumar, Angiogenesis induced by degradation products of hyaluronic acid, Science 228 (1985) 1324–1326.
- [71] D.R. Griffin, W.M. Weaver, P.O. Scumpia, D. Di Carlo, T. Segura, Accelerated wound healing by injectable microporous gel scaffolds assembled from annealed building blocks, Nat. Mater. 14 (2015) 737–744.
- [72] J.M. de Rutte, J. Koh, D. Di Carlo, Scalable high-throughput production of modular microgels for in situ assembly of microporous tissue scaffolds, Adv. Funct. Mater. 29 (2019) 1900071.
- [73] J. Koh, D.R. Griffin, M.M. Archang, A. Feng, T. Horn, M. Margolis, D. Zalazar, T. Segura, P.O. Scumpia, D. Carlo, Enhanced *in vivo* delivery of stem cells using microporous annealed particle scaffolds, Small 15 (2019) 1903147.
- [74] P.C. Georges, W.J. Miller, D.F. Meaney, E.S. Sawyer, P.A. Janmey, Matrices with compliance comparable to that of brain tissue select neuronal over glial growth in mixed cortical cultures, Biophys. J. 90 (2006) 3012–3018.
- [75] T.H. Qazi, V.G. Muir, J.A. Burdick, Methods to characterize granular hydrogel rheological properties, porosity, and cell invasion, ACS Biomater. Sci. Eng. 8 (2022) 1427–1442.
- [76] N.F. Truong, E. Kurt, N. Tahmizyan, S.C. Lesher-Pérez, M. Chen, N.J. Darling, W. Xi, T. Segura, Microporous annealed particle hydrogel stiffness, void space size, and adhesion properties impact cell proliferation, cell spreading, and gene transfer, Acta Biomater. 94 (2019) 160–172.
- [77] J. Kim, K.S. Kim, G. Jiang, H. Kang, S. Kim, B.S. Kim, M.H. Park, S.K. Hahn, *In vivo* real-time bioimaging of hyaluronic acid derivatives using quantum dots, Biopolymers 89 (2008) 1144–1153.
- [78] T.H. Qazi, L. Tytgat, P. Dubruel, G.N. Duda, S. Van Vlierberghe, S. Geissler, Extrusion printed scaffolds with varying pore size as modulators of MSC angiogenic paracrine effects, ACS Biomater. Sci. Eng. 5 (2019) 5348–5358.
- [79] O. Oliviero, M. Ventre, P.A. Netti, Functional porous hydrogels to study angiogenesis under the effect of controlled release of vascular endothelial growth factor, Acta Biomater. 8 (2012) 3294–3301.
- [80] A.E. Haggerty, I. Maldonado-Lasunción, M. Oudega, Biomaterials for revascularization and immunomodulation after spinal cord injury, Biomed. Mater. 13 (2018) 044105.

- [81] U. Graumann, M.F. Ritz, O. Hausmann, Necessity for re-vascularization after spinal cord injury and the search for potential therapeutic options, Curr. Neurovasc. Res. 8 (2011) 334–341.
- [82] Y. Wen, S. Yu, Y. Wu, R. Ju, H. Wang, Y. Liu, Y. Wang, Q. Xu, Spinal cord injury repair by implantation of structured hyaluronic acid scaffold with PLGA microspheres in the rat, Cell Tissue Res. 364 (2016) 17–28.
- jury repair by implantation of structured hydrotonic acid scalloid with PLGA microspheres in the rat, Cell Tissue Res. 364 (2016) 17–28.

 [83] D. Jiang, J. Liang, J. Fan, S. Yu, S. Chen, Y. Luo, G.D. Prestwich, M.M. Mascarenhas, H.G. Garg, D.A. Quinn, R.J. Homer, D.R. Goldstein, R. Bucala, P.J. Lee, R. Medzhitov, P.W. Noble, Regulation of lung injury and repair by Toll-like receptors and hyaluronan, Nat. Med. 11 (2005) 1173–1179.
- [84] S.C. Wu, C.H. Chen, J.Y. Wang, Y.S. Lin, J.K. Chang, M.L. Ho, Hyaluronan size alters chondrogenesis of adipose-derived stem cells via the CD44/ERK/SOX-9 pathway, Acta Biomater. 66 (2018) 224–237.
- [85] T.J. Lambert, FPbase: a community-editable fluorescent protein database, Nat. Methods 16 (2019) 277–278 2019 16:4..
- [86] D. Morzy, M. Bastings, Significance of receptor mobility in multivalent binding on lipid membranes, Angew. Chem. Int. Ed. 61 (2022) e202114167.
 [87] S.J. Lord, K.B. Velle, R.D. Mullins, L.K. Fritz-Laylin, SuperPlots: Communications.
- [87] S.J. Lord, K.B. Velle, R.D. Mullins, L.K. Fritz-Laylin, SuperPlots: Communicating reproducibility and variability in cell biology, J. Cell Biol. 219 (2020) e202001064.